NASA Contractor Report 198523

Impingement-Current-Erosion Characteristics of Accelerator Grids on Two-Grid Ion Thrusters

Timothy Barker
Colorado State University
Fort Collins, Colorado

August 1996

Prepared for
Lewis Research Center
Under Grant NAG3–1801

National Aeronautics and
Space Administration

REPORT DOCUMENTATION PAGE

Form Approved
OMB No. 0704-0188

1. AGENCY USE ONLY *(Leave blank)*

2. REPORT DATE
August 1996

3. REPORT TYPE AND DATES COVERED
Final Contractor Report

4. TITLE AND SUBTITLE
Impingement-Current-Erosion Characteristics of Accelerator Grids on Two-Grid Ion Thrusters

5. FUNDING NUMBERS
WU–233–1B–1B
G–NAG3–1801

6. AUTHOR(S)
Timothy Barker

7. PERFORMING ORGANIZATION NAME(S) AND ADDRESS(ES)
Colorado State University
Mechanical Engineering Department
Fort Collins, CO 80523–1374

8. PERFORMING ORGANIZATION REPORT NUMBER
E–10411

9. SPONSORING/MONITORING AGENCY NAME(S) AND ADDRESS(ES)
National Aeronautics and Space Administration
Lewis Research Center
Cleveland, Ohio 44135–3191

10. SPONSORING/MONITORING AGENCY REPORT NUMBER
NASA CR–198523

11. SUPPLEMENTARY NOTES

Project Manager, Vincent K. Rawlin, Space Propulsion Technology Division, NASA Lewis Research Center, organization code 5330, (216) 977–7462.

12a. DISTRIBUTION/AVAILABILITY STATEMENT
Unclassified - Unlimited
Subject Categories 20 and 18

This publication is available from the NASA Center for AeroSpace Information, (301) 621–0390.

12b. DISTRIBUTION CODE

13. ABSTRACT ***(Maximum 200 words)***

Accelerator grid sputter erosion resulting from charge-exchange-ion impingement is considered to be a primary cause of failure for electrostatic ion thrusters. An experimental method was developed and implemented to measure erosion characteristics of ion-thruster accel-grids for two-grid systems as a function of beam current, accel-grid potential, and facility background pressure. Intricate accelerator grid erosion patterns, that are typically produced in a short time (a few hours), are shown. Accelerator grid volumetric and depth-erosion rates are calculated from these erosion patterns and reported for each of the parameters investigated. A simple theoretical volumetric erosion model yields results that are compared to experimental findings. Results from the model and experiments agree to within 10%, thereby verifying the testing technique. In general, the local distribution of erosion is concentrated in pits between three adjacent holes and trenches that join pits. The shapes of the pits and trenches are shown to be dependent upon operating conditions. Increases in beam current and the accel-grid voltage magnitude lead to deeper pits and trenches. Competing effects cause complex changes in depth-erosion rates as background pressure is increased. Shape factors that describe pits and trenches (i.e. ratio of the average erosion width to the maximum possible width) are also affected in relatively complex ways by changes in beam current, accel-grid voltage magnitude, and background pressure. In all cases, however, gross volumetric erosion rates agree with theoretical predictions.

14. SUBJECT TERMS
Electrostatic ion thruster; Impingement current; Charge-exchange ions

15. NUMBER OF PAGES
00

16. PRICE CODE
A00

17. SECURITY CLASSIFICATION OF REPORT	**18. SECURITY CLASSIFICATION OF THIS PAGE**	**19. SECURITY CLASSIFICATION OF ABSTRACT**	**20. LIMITATION OF ABSTRACT**
Unclassified	Unclassified	Unclassified	

Table of Contents

List of Tables

List of Figures

I. Introduction

In recent years, electric propulsion (EP) has become a viable alternative to traditional chemical systems for many space propulsion applications. Specifically, ion thrusters are attractive because they utilize low propellant flow rates and very high exhaust velocities (i.e. high specific impulses), and this leads to improved performance compared to chemical thrusters for some missions. Initially, ion thrusters were investigated for use on interstellar missions [1], interplanetary and comet rendezvous missions [2,3], and orbit raising missions [4]. With advances in EP technologies, however, ion thrusters also appear to be attractive for many north-south station keeping [5] and low earth orbit (LEO) to geosynchronous earth orbit (GEO) missions [4]. All of the attractive benefits of ion thrusters in space applications, however, are achieved at certain costs. Operation at a very low propellant flow rates results in thrust levels which are very small, (typically tens to a few hundred milli-newtons)[6] and this can make the times required to complete some missions much greater than those for chemical rockets. For example, the vigorous mission of rendezvousing with comet Encke, requires 15,000 hours of continuous ion thruster operation [2]. With typical mission operating times over 10,000 hours, keeping all the components of an ion thruster functioning can be a daunting task. To understand possible ion thruster failure mechanisms, knowledge of ion thruster operation is essential.

The components needed to generate thrust in a typical ion thruster, which are shown in Fig. 1 include 1) a discharge chamber, 2) a hollow cathode, 3) an anode, 4) screen and accelerator (accel) grids, and 5) a neutralizer. A propellant, typically xenon, is fed into the discharge chamber and into the hollow cathode containing a low-work-function, electron-emitting insert. Some of the xenon propellant flows through the orifice plate attached to the end of the cathode but the bulk of it flows directly into the chamber. Electrons emitted from the insert are accelerated to modest kinetic energies by a potential difference applied between the cathode and the anode (the electron collecting surface). Accelerated electrons collide with the neutral xenon atoms within the discharge chamber, thereby inducing ionization. Hence, every ionization collision yields one ion and its ejected electron, in addition to the original electron which loses energy in the collision. The ionization-ejected electron and original electron frequently will not have enough energy to ionize any additional xenon atoms and will, after some additional collisions, be removed from the discharge chamber at the anode. The continual creation of ions and electrons within the discharge chamber yields a discharge plasma. Many of the ions within this plasma migrate toward the ion extraction electrodes (i.e. the screen and accel grids or the grid set). These two grids are typically two convex plates perforated by numerous aligned apertures. Typically, the screen grid is connected electrically to the discharge chamber, and the accel grid is isolated from both the screen grid and discharge chamber as shown in Fig. 1. When a positive potential generally on the order of a thousand volts is applied to the screen grid and discharge chamber while a negative potential on the order of a few hundred volts is

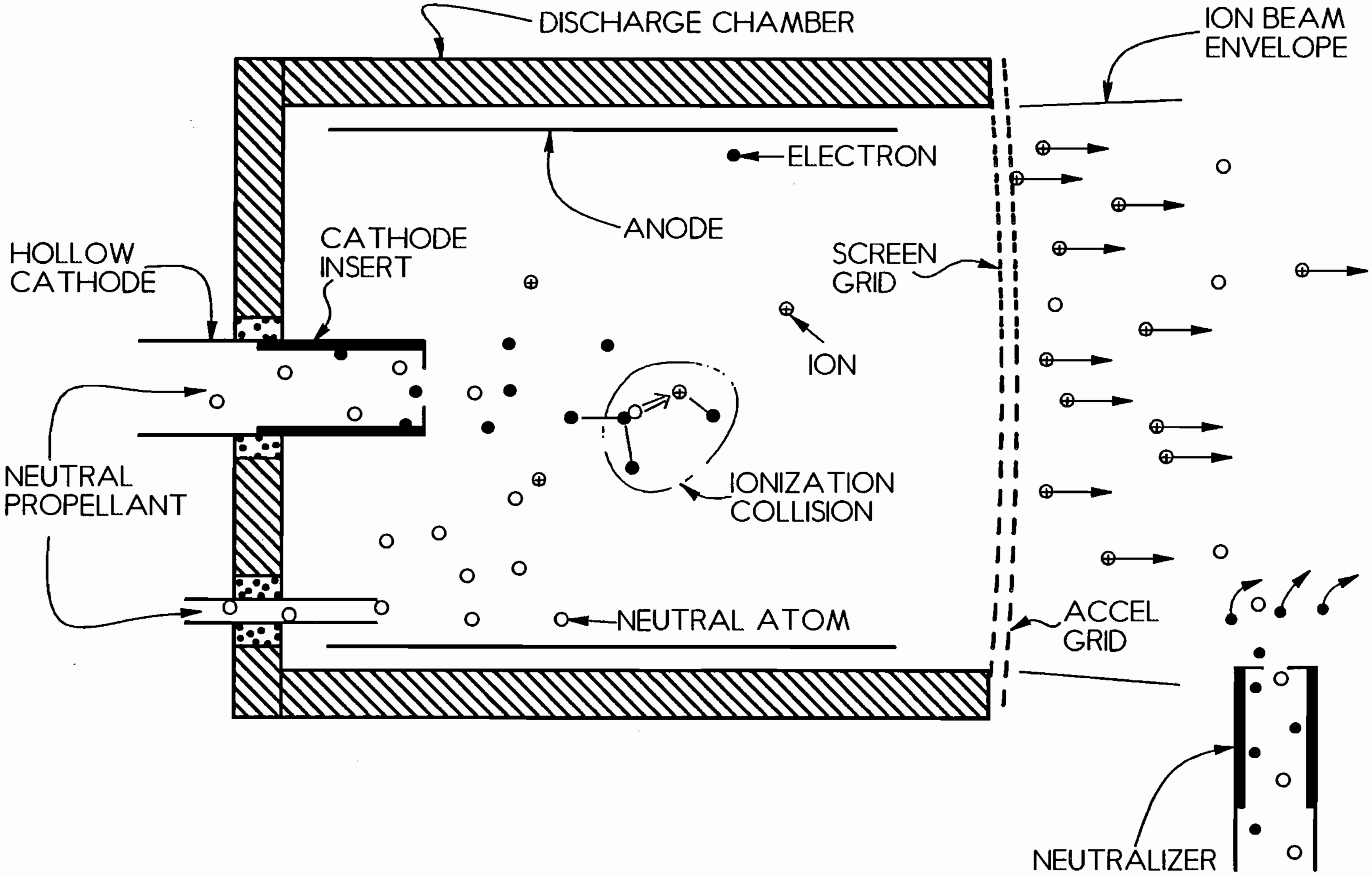

Fig. 1 Schematic Drawing of an Ion Thruster

applied to the accel grid, a beam of the ions produced in the discharge chamber will be extracted. The acceleration of these ions begins as they migrate toward the screen grid and feel the attractive influence of the accel grid. As a result of this acceleration, the ions in the beam have velocity vectors (shown as arrows in Fig. 1) that are directed downstream and are generally confined within an ion-beam envelope like that suggested in Fig. 1. It is possible that the accelerated ions leaving the discharge chamber will strike the accel grid if the apertures are not correctly aligned or the thruster is operated improperly. This impact on the accel grid is termed direct impingement and with proper design and operation it can be reduced to a negligible level.

It is important to recognize that electrons will not be lost through the grid set. Hence, a steady current of ions leaving the discharge chamber could cause the thruster and the circuitry connected to it to charge negatively. To eliminate this problem, a neutralizer similar in design to the main hollow cathode is operated and it serves to eject electrons into the ion beam at a rate equal to the ion extraction rate to assure no net charging of the spacecraft.

Ion thruster testing has revealed that thruster failure can occur because material is eroded from the accel grid to the point where it fails structurally [7,8,9,10]. This type of failure occurs as a result of ions produced at or downstream of the grids in the ion beam which move upstream (counter to the higher velocity beam ions). These ions strike the accel grid and erode it through the sputter-erosion process. The objective of this thesis is to determine the effect of thruster operating parameters on this erosion process.

II. Development of Accel-Grid Erosion Model

A. Impingement Current Production

Figure 2 shows a sketch of a single screen/accel grid aperture pair and a typical potential profile along the centerline of these apertures. The electrons, ions, and neutral atoms to the left of the sheath (i.e. in the discharge chamber) are each moving at their respective thermal speeds when they are far from the sheath. As they migrate through the sheath, they pass from a plasma at a uniform potential within the discharge chamber into a region of steep electrical potential gradient created by the screen and accel grids. At the sheath, ions begin their downstream acceleration and the electrons are reflected back into the discharge chamber. Neutral propellant atoms, having no net charge, also pass downstream through the sheath but they are unaffected by the potential gradient there. As shown in Fig. 2a, ions move through the ion acceleration region (Fig. 2b) and gain kinetic energy (shown by longer velocity vectors) generally without interacting with the neutral propellant atoms which are just drifting through this region. These two particle species, however, do occasionally undergo a charge-exchange collision (shown in Fig. 2a). A charge-exchange collision involves the transfer of an electron from the slow-moving neutral propellant atom to the fast-moving beam ion. This transfer results in a charge-exchange ion with the low energy of the pre-collision neutral atom and an atom with the high energy of the pre-collision beam

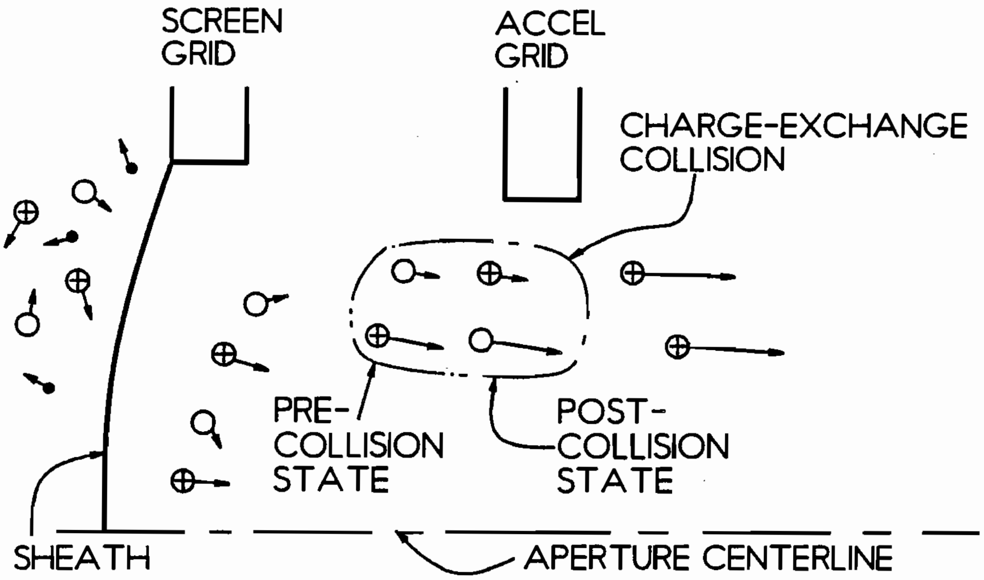

a. Single Aperture Pair

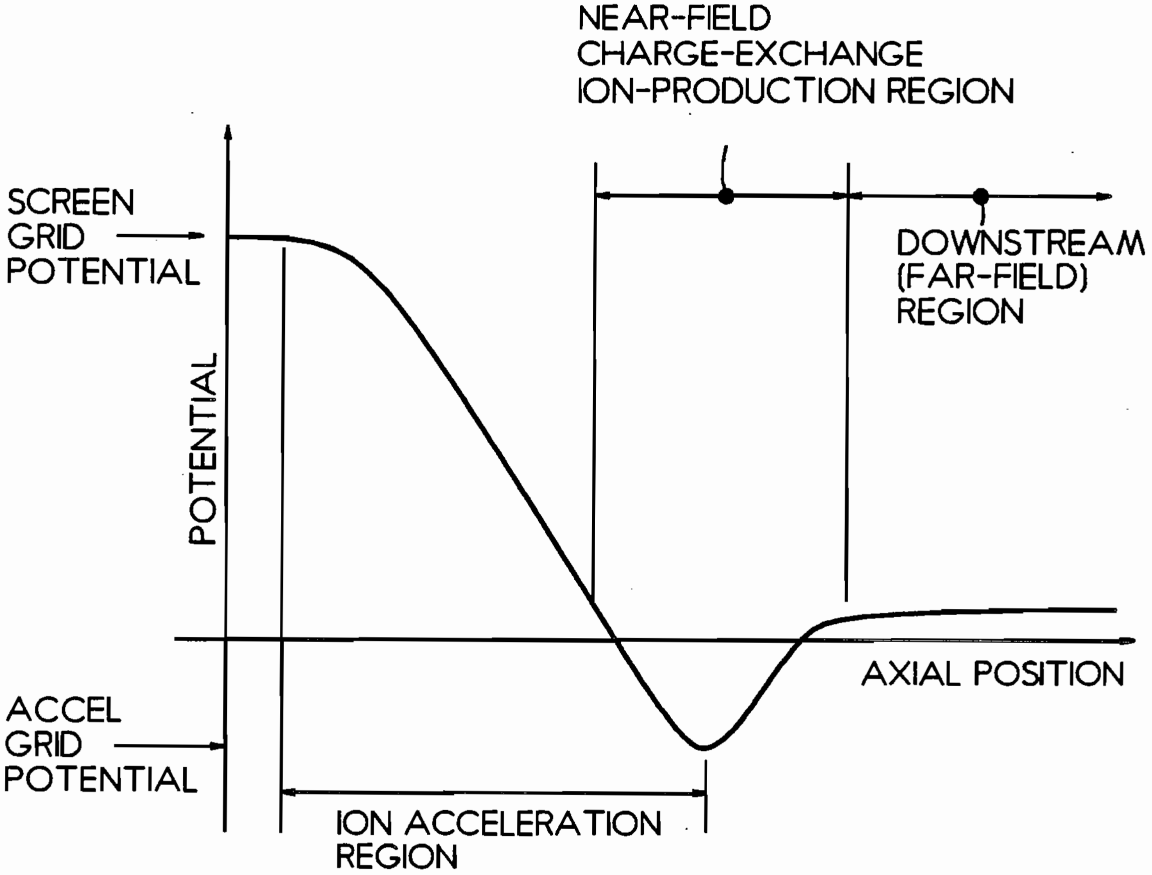

b. Corresponding Centerline Potential Profile Through Aperture Pair

Fig. 2 The Influence of Beam and Charge-Exchange Ion Motion

ion. Both beam and near-field charge-exchange ions reach their maximum kinetic energies near the accel grid and then undergo a slight deceleration as they exit the ion-acceleration region. Beam ions have sufficient kinetic energy to escape this potential deceleration well, while the lower energy near-field charge-exchange ions typically do not. Therefore, all of the charge-exchange ions created within the near-field charge-exchange ion-production region will strike, or impinge on the accel grid and cause sputter erosion. Beam ions and the charge-exchange ions created upstream of the near-field charge-exchange ion-production region escape the accel-grid potential well and enter the downstream ambient plasma with kinetic energies determined by either the screen-grid potential or the potential at which the charge-exchange ions were created. As beam ions and neutral particles proceed into the downstream (far-field) region, it is possible for further charge-exchange collisions to occur. Work conducted by Monheiser [11] has shown that there is a finite probability that charge-exchange ions created in this downstream region will also impinge upon the accel grid.

B. Accel-Grid Erosion Model

The two different charge-exchange ion-impingement production mechanisms (near and far field) both yield ions that have energies associated with the potential difference between that at the point where they are produced and that of the accel grid. These energies are generally sufficient to cause sputter erosion which is typically non-uniform over the accel-grid surface, and for a two-grid system generally occurs on the downstream surface of this grid. Erosion of the downstream grid surface, which can limit the life of an ion thruster, yields charge-exchange-ion erosion patterns on the downstream side of an accel grid that are like that shown in Fig. 3. Notice the non-uniform, hexagonal-shape accel-grid erosion occurring around each hole. The nature of the non-uniform erosion that occurs around an aperture surrounded by six others is illustrated in the sketch of Fig. 4, which shows idealized erosion patterns. As the figure suggests, the basic erosion structure involves pits which develop between three adjacent apertures and trenches which join each pair of pits. There is a region close to each hole where the erosion is mild and as the erosion proceeds, a relatively uneroded mesa around each hole remains.

The pit that develops between any three apertures can be ideally represented by the frustrum of an inverted right circular cone with diameters d_1, d_2 and height h_p. Trench erosion occurs between any two pits and can be represented as trapezoidal in cross section with larger and smaller bases that have widths w_T and w_2, respectively, and a length ℓ_T. The cross-sectional views along A-A′ and B-B′ show the idealized shapes of the pit-cone frustra and a trapezoidal trench. Assuming erosion conditions are uniform throughout a test, depth-erosion rates associated with the pits and trenches are found by dividing the corresponding depths of erosion by the time (t) the accel-grid was exposed to impinging ions. These erosion rates are considered to be critical when describing thruster lifetimes. In particular, when the trench has been eroded through the entire accel-grid thickness, failure of the ion thruster can occur because the material within the hexagonal erosion pattern is no longer attached to the accel grid and this section can fall into the screen grid and establish an electrical short between the two

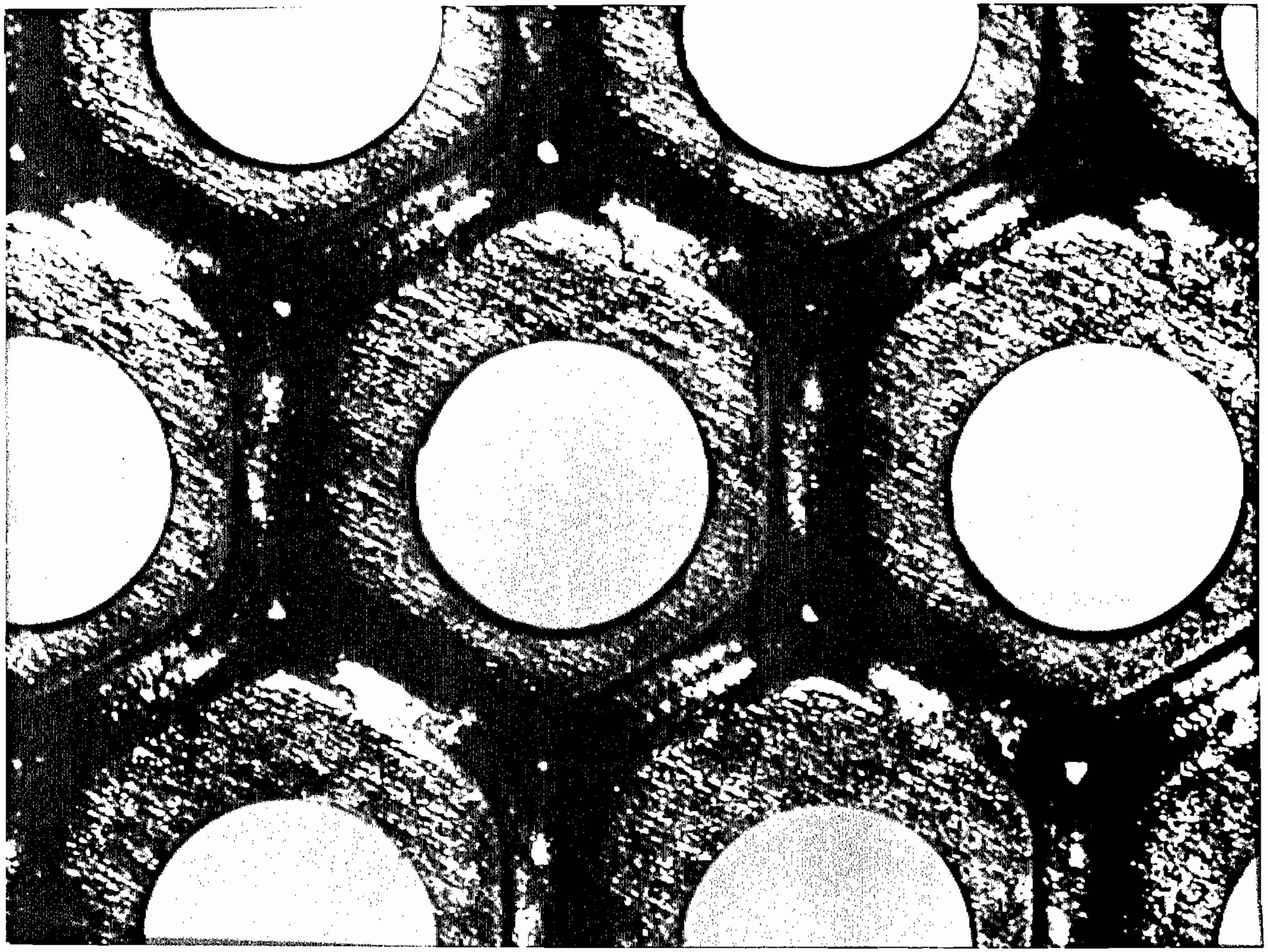

Fig. 3 Charge-Exchange-Ion Erosion Pattern on the Downstream Side of an Accelerator Grid
(photo courtesy of NASA Lewis)

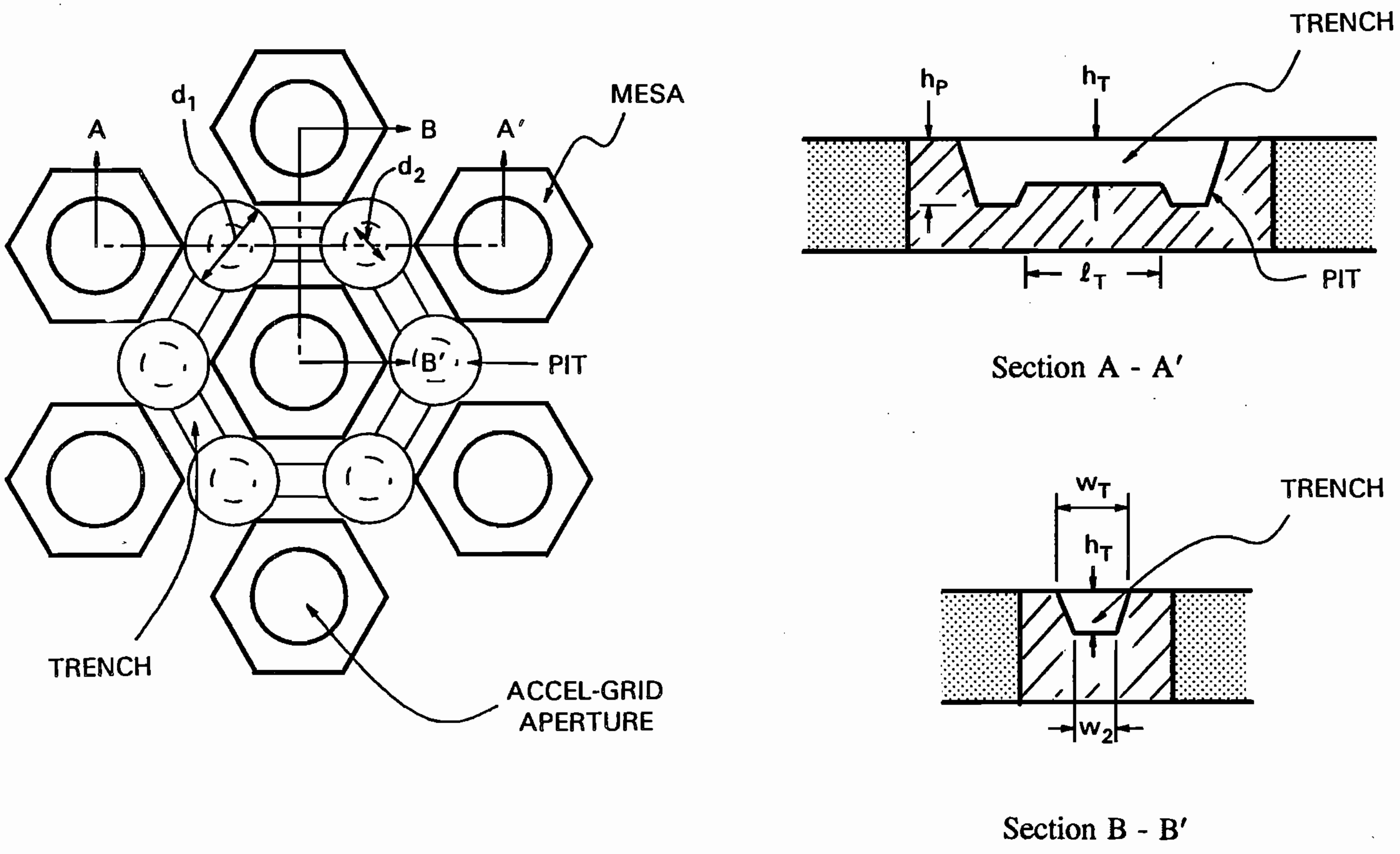

Section A - A′

Section B - B′

Fig. 4 Idealized Accelerator Grid Erosion Patterns grids. This occurrence is generally regarded as the end of life for the thruster.

It is worthwhile to examine what factors determine the depth-erosion rates within the pits and trenches. The critical depth-erosion rate (the one yielding the most rapid erosion in a trench) is dependant on the peak impingement current density (j_i) at that location. This maximum depth-erosion rate $(dx/dt)_{max}$ is given in Eq. 1 as the product of the peak-impingement-current density and several other parameters.

$$\left(\frac{dx}{dt}\right)_{max} = \frac{j_i S(\epsilon) m_A}{e\rho} \quad (1)$$

The variables $S(\epsilon)$, m_A and ρ are the sputter yield for ions with kinetic energy ϵ, atom mass, and density, respectively associated with the grid material. The constant e is the charge of an election. It is desirable to express the peak-current density in Eq. 1 in terms of the accel-grid total impingement current because the total impingement current is measured readily. This is achieved through the use of two factors, δ and f. Delta (δ) is defined as the ratio of the current that impinges on the accel grid outside of the ion-beam envelope to the total impingement current. Since pits and trenches only occur within the ion-beam envelope where there are apertures, this factor is needed to assure that erosion due to impingement current within the ion-beam envelope only is considered. The impingement current density uniformity factor (f) is defined as the ratio of the average-impingement-current density (within the ion-beam envelope) to the peak-impingement-current density within a trench or pit. Incorporation these factors into Eq. 1, one obtains

$$\left(\frac{dx}{dt}\right)_{max} = \frac{J_i(1-\delta)S(\epsilon)m_A}{Afe\rho}\,, \tag{2}$$

where J_i is the total impingement current, and A is the area of the accel-grid material within the active beam region. Equation 2 is useful for illustrating the effects of ion-thruster operating conditions on depth-erosion rates and it will be cited frequently. An assumption inherent in Eq. 2 is that material sputtered from other locations on the accel grid does not re-deposit at the location of maximum sputter erosion rate. In this analysis both the effects of deposition of material sputtered from other locations and changes in sputter yield with changes in surface contour are neglected.

The volumetric erosion rate associated with the grid material is of interest because it can be computed from two quantities that can be measured readily (the eroded volume and the test duration). It can also be computed directly from the impingement current without the complication of the factors that appear in Eq. 2. For grids made of material with uniform properties, erosion volumes can be calculated for pits and trenches in the active beam region and in the peripheral area outside this region. The following erosion volume equations are derived in detail as functions of accel-grid geometry in Appendix A. Using the terminology presented in Fig. 4, the volume eroded from a total number of pits N_p is given by

$$V_{pits} = N_p\left[\frac{1}{12}\pi h_p(d_2^2+d_1d_2+d_1^2)\right] \tag{3}$$

and the volume eroded from a total number of trenches N_T is given by

$$V_{\text{trenches}} = N_T\left[\frac{1}{2}\ell_T h_T (w_T + w_2)\right] . \tag{4}$$

The area on the accel grid within tangent lines that circumscribe the outer-most apertures is defined as the active beam area. Periphery erosion which occurs outside of this area can also be substantial. The equation used to model periphery erosion volumes is found to be dependant on accel-grid geometry and is also developed in Appendix A.

The total volume eroded in a time t is the sum of the pit, trench and periphery volumes. For a homogeneous grid material this total volume of material removed per unit time can be calculated independently using the measured impingement current (J_i) in the equation

$$\frac{V}{t} = \frac{S(\epsilon) m_A J_i}{e \rho} , \tag{5}$$

where t is the time the accel-grid is exposed to the impinging ions. The volume rate computed using Eq. 5 can be compared to the rate determined from the test time and the sum of erosion volumes of pits (determined using Eq. 3), trenches (determined using Eq. 4) and periphery (modeled in Appendix A). If all of the material that is sputtered leaves the grids, the sputtering on the upstream side of the accel-grid and hole-barrel surfaces are negligible and the model inherent in Eq. 5 is correct, the sum of the computed volumes should agree with the value given by Eq. 5.

It is desirable to relate the trench-depth erosion rate, which defines the lifetime of a grid, to the total volume (or mass) loss rate which can be determined readily from the measured impingement current using Eq. 5. These rates are directly relatable through Eqs. 2 and 5 to the extent that the factors δ and f are known. The ratio of the depth-erosion rate at a particular location to the total volumetric-erosion rate obtained by combining these equations (i.e. Erosion Proportion Factor P) is given by

$$P = \frac{(dx/dt)}{(V/t)} = \frac{1-\delta}{Af} . \qquad (6)$$

An objective of this thesis is to show the effects of changes in beam current, accel-grid potential and ambient pressure on total impingement current, volumetric erosion rate and pit and trench depth-erosion rates. This will enable both the validation of Eq. 5 and the determination of the quantities P, δ, and f in Eq. 6.

III. Experimental Apparatus and Procedure

A. Testing Method

Erosion patterns produced on the downstream surfaces of accel grids by charge-exchange ions that impinge on them can be measured by applying thin multi-layer coatings to these surfaces. This multi-layer erosion measurement method was developed at Hughes Research Laboratories to measure erosion rates over short test intervals [12]. Because the coatings are thin, they erode relatively rapidly and if alternating layers are different colors, grid erosion patterns can be seen visually after short periods of operation (several hours). The grid sets used in the tests had nineteen holes arranged in a hexagonal pattern, with equal hole-to-hole spacings, in both the screen and accel grids. This testing procedure involved 1) coating an accel grid with multiple, thin alternating layers of metals that were different colors, 2) operating a thruster at constant conditions with the coated grid installed, 3) photographically recording the accel grid sputter-erosion pattern produced by the charge-exchange ions, and 4) using the known layer thicknesses to establish erosion depths as a function of position on the grid.

Ion thruster grid sets with 19-Hole SHAG (Small Hole Accelerator Grid) configurations, having the same hole pattern as typical operational grid sets [7,8,9,10], were constructed from a stainless steel sheet with the hole pattern shown in Figure 5.

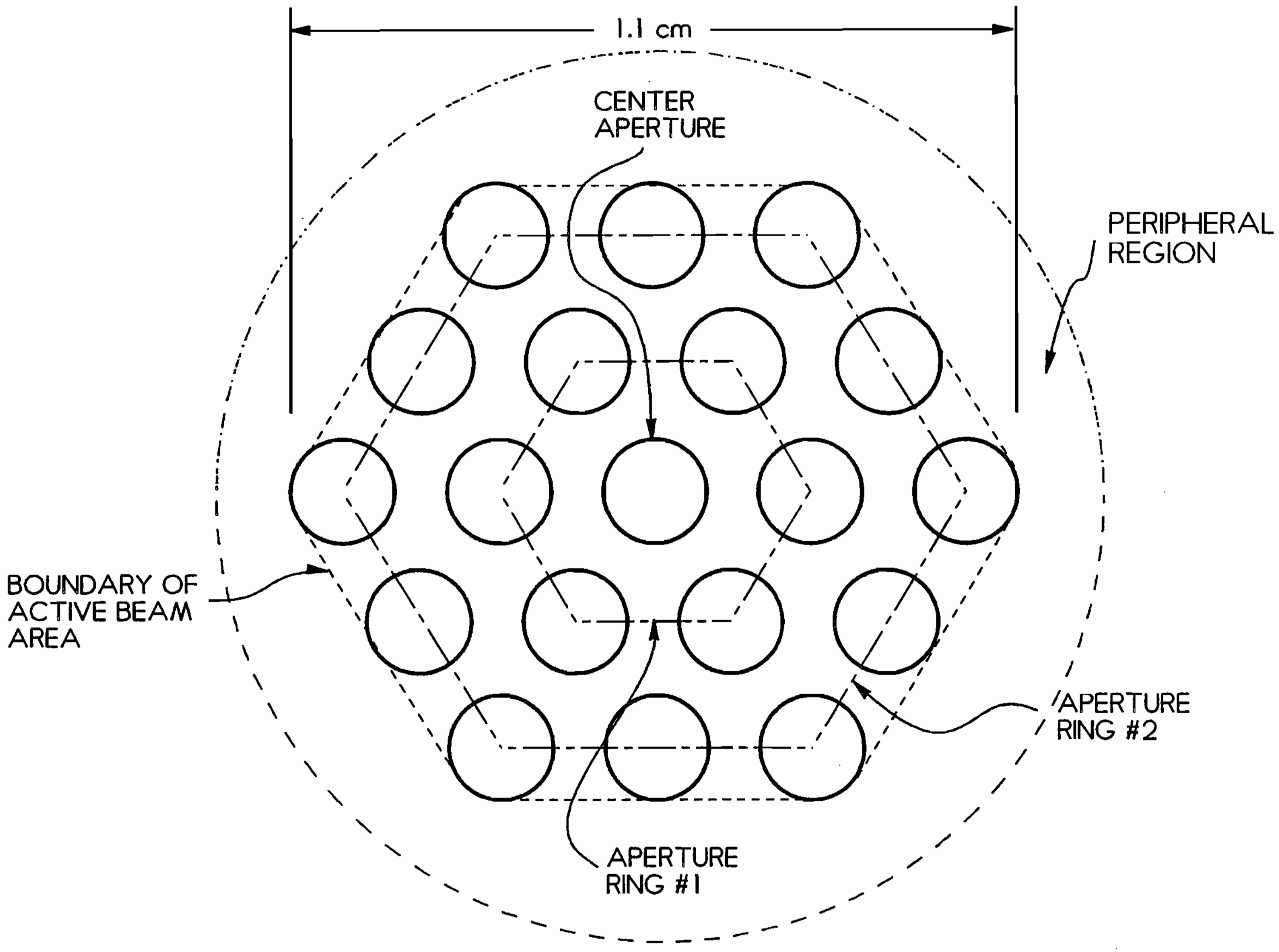

Fig. 5 Nineteen-Hole SHAG Geometry

Erosion occurs within the dashed circle, but the region of principal interest here is within the dotted line that bounds all of the apertures and is designated as the active beam area. In addition to the center aperture, there are two rings of apertures identified in Fig. 5, namely those in ring #1 that are completely surrounded by apertures and those in the outer ring (#2) and, therefore, are not. Dimensions associated with the 19-Hole SHAG grid set used in this study are presented in Table 1. Only nineteen aperture pairs were used because 1) the pattern around the central hole appeared to be representative of holes far from the periphery of an actual thruster grid, 2) the grids could be constructed inexpensively, and 3) they enabled thruster operation at low flow rates and, therefore, low facility background pressures. Nineteen hole grid sets were also used because they yielded a beam diameter that was small compared to the diameter of the thruster, and as a consequence, the current should have been the same through each hole.

After machining the grids from AISI 304 stainless steel sheet metal, they were prepared for testing by polishing and sputter coating them with thin alternating layers of copper (Cu) and AISI 303 stainless steel (SS). The coating procedure involved first sputter cleaning the stainless steel grid and then applying twelve alternating ~500 Å layer coatings of the copper and stainless steel (six of each) onto the downstream face of each accel grid. The sputter cleaning and coating of the accel grid was accomplished sequentially using the 15-cm diameter, ion-beam sputter coating system [13] shown schematically in Fig 6. The ion source was consistently operated on argon at an energy of 1 keV and a beam-ion current density of 2 mA/cm^2.

Table 1

Summary of Nineteen-Hole SHAG Set Parameters

Screen-Aperture Diameter (mm)	1.98
Accel-Aperture Diameter (mm)	1.47
Screen-Grid Thickness (mm)	0.25
Accel-Grid Thickness (mm)	0.25
Grid Spacing (mm)	0.66
Screen-Grid Open-Area Fraction	0.61
Accel-Grid Open-Area Fraction	0.34

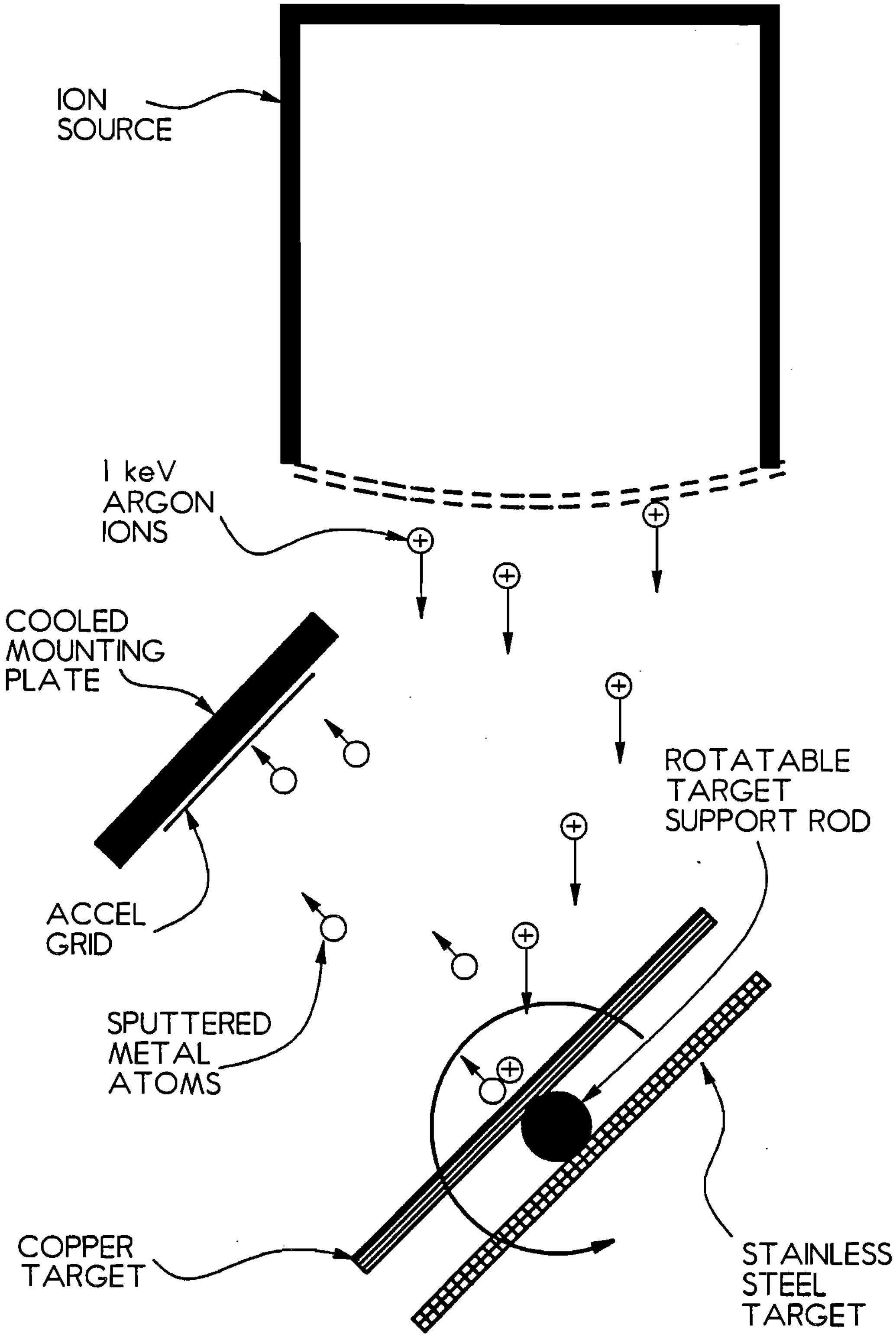

Fig. 6 Sputter Coating System

The stainless steel grid and cooled mounting plate were first placed directly in the ion beam for ~10 seconds to sputter clean the accel-grid surface. Next, the accel grid and mounting plate were rotated out of the beam and placed in the position shown in Fig. 6. In this position, ions extracted from the ion-source are accelerated through the grid set and bombard the copper target, causing it to sputter erode copper metal atoms onto the grid. This process is continued until a 500 +/- 15 Å coating has been applied (~1 minute). The target support rod is then rotated so the stainless steel target is in the ion beam, and constituent atoms of stainless steel will be sputtered onto the accel grid. Again, this process is continued until ~500 +/- 15 Å has been deposited (~1.5 minutes) onto the accel grid. This process is repeated, rotating the target support rod back and forth until all twelve layers have been deposited (~15 min).

The times required to deposit 500 Å of each material were determined by sputter coating glass slides which were partially covered by a thin mask strip (~2 mm wide) and then mounted to the cooled mounting plate shown in Fig. 6. Specifically, copper or stainless steel was sputtered onto the glass slide using the ion source (Ar @ 1keV, 2mA/cm^2) for ~20 minutes. The mask strip was then removed from the glass slide and the sputter coating thickness (the height between glass substrate and the top of the coating surface) was measured using a stylus profilometer. Coating rates were determined by dividing this thickness by the coating time (20 min.). This rate, in conjunction with the desired coating thickness of 500 Å, was used to establish the stainless steel and copper sputter coating times.

After coating, a grid set was installed on a Space Electric Rocket Test II (SERTII) ion-thruster [14] which had been modified to accept these nineteen aperture grid sets. This thruster has also been modified so it can be operated on inert gases (eg. xenon) with flow rates through the body and cathode independently controlled. During these tests, cathode flow alone at ~0.5 sccm (standard cubic centimeters per minute) of xenon yielded the flow conditions that enabled operation at the desired conditions for the nineteen hole grids, and no body flow was needed.

The SERT II thruster was operated using the power supplies shown schematically in Fig. 7. With the cathode flow established, the hollow cathode heater supply was used to heat a low-work-function cathode insert within the hollow cathode to the temperature at which it would emit electrons. Most of these electrons were accelerated near the cathode through the discharge potential (V_D) and would acquire sufficient energy to collide with and ionize xenon propellant atoms in the discharge chamber. The keeper serves to sustain the electrical discharge in the chamber and a small current (J_k) of electrons from the cathode and discharge chamber is collected on it. Most of the electron current is, however, collected on the anode and is designated the discharge current (J_D). Ions produced within the discharge chamber are extracted to form the ion beam using the screen and accel-grid power supplies. This ion extraction current is measured by the beam current (J_B) ammeter and is dependant on the grid voltages and other operating parameters. At a condition established by the accel and screen grid voltages and the beam current, the sheath (Fig. 2a) surface area will adjust itself such that the proper current of ions will undergo the acceleration process. Recall

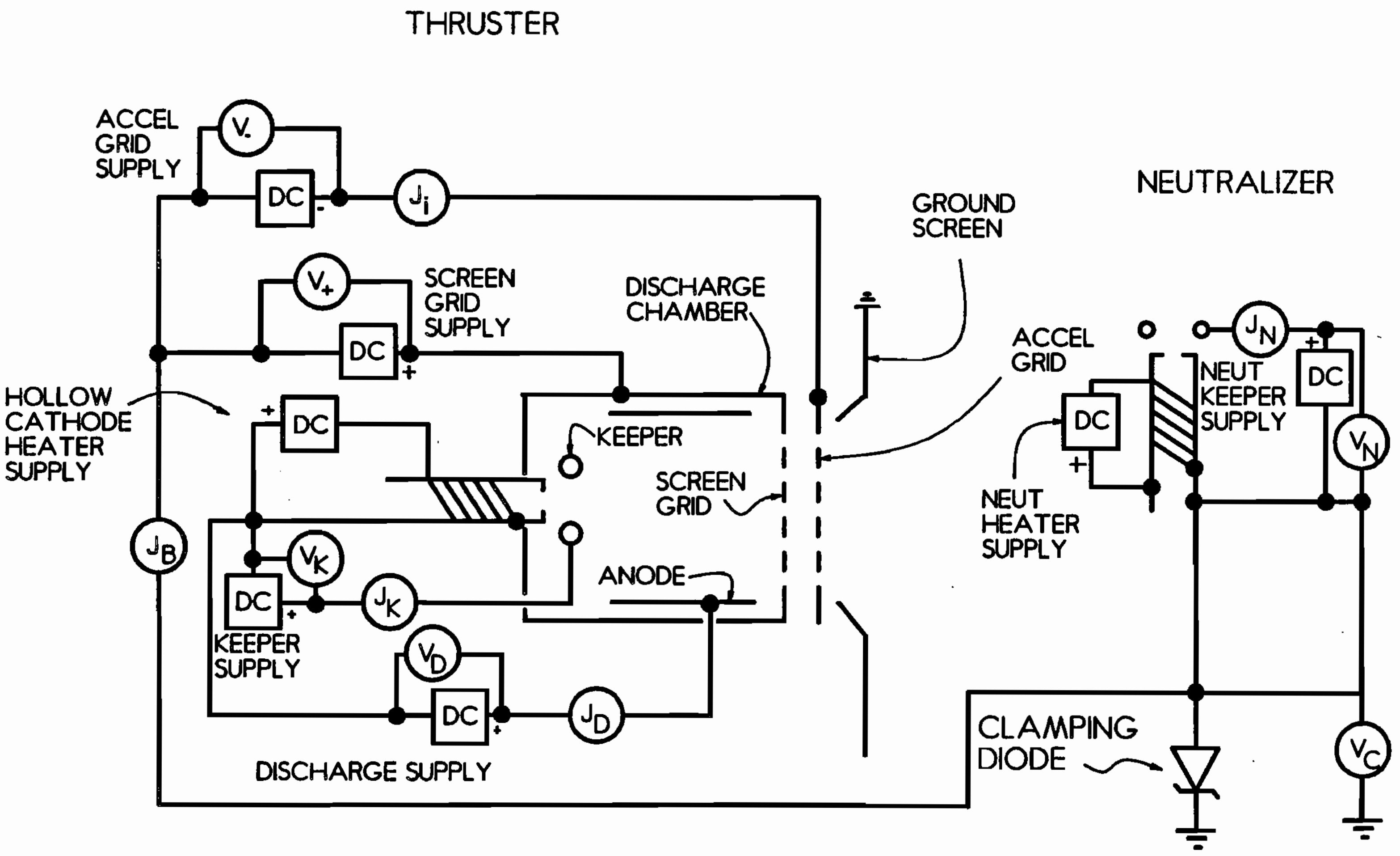

Fig. 7 Ion-Thruster Electrical Schematic

that these accelerated beam ions pass through the aperture set, occasionally producing charge-exchange ions from some of the neutral atoms present. These charge-exchange ions are collected on the accel grid at a rate which is measured by the impingement current ammeter (J_i).

The ion thruster neutralizer was consistently placed ~20 cm downstream of the ground screen, ~12 cm from the thruster centerline. The power supplies for the neutralizer are very similar to the main cathode supplies with the neutralizer keeper current (J_N) sustained by the neutralizer keeper supply. The neutralizer floats at the potential relative to ground (V_c) that assures the total electron flow from the neutralizer cathode is equal to the ion-beam current (J_B). The zener diode shown between the neutralizer common line and ground serves to isolate the neutralizer from ground unless the neutralizer potential exceeds the zener voltage set point. In this case the diode passes the current needed to prevent further charging.

All the experiments were conducted with the thruster mounted on centerline at one end of a 1.2 m-dia. by 5.4 m-long stainless steel tank that was evacuated by a 91 cm-diameter diffusion pump in series with a Roots blower and a rotary, piston-type vacuum pump. Ambient vacuum tank pressure was measured using a Schultz-Phelps type, hot-filament ionization gauge [15] located approximately one meter downstream of the thruster. Under no-flow conditions, the pumps produced tank pressures in the low 10^{-6} Torr range. During background pressure tests, it was necessary to raise facility pressures above the nominal level. These higher background pressures were achieved by throttling the diffusion pump using a stainless steel plate that could be slid over the pump intake during operation and/or by backfilling with the propellant used (Xe) at a remote location (~2.5 m downstream of the thruster).

Since accel-grid erosion is directly proportional to impingement current (Eq. 5), it is desirable to examine the effects of critical operating conditions on this current. Specifically, impingement current was measured as beam current, background pressure, and accel-grid voltage were independently varied. Results from these tests are presented to show general expected trends in accel-grid volumetric erosion rate with changes in operating conditions.

To examine in detail the effects of operating condition on accel-grid erosion, coated grids were installed on the SERT II thruster and tested at a specified beam current, background pressure, and accel-grid voltage condition. Screen-grid voltage was always held constant at +1000 V, and the discharge current, and therefore discharge voltage, were varied to produce the desired beam current. After operating the thruster for enough time to produce erosion patterns on the accel grid, the grid set would be removed from the thruster for documentation and analysis. A new coated grid would then be installed and the process would be repeated for each different operating condition. Three different parameters namely 1) beam current (J_B), 2) background pressure (P_O), and 3) accel-grid voltage (V_-) were varied independently in the tests. Operation was maintained at various beam currents while accel-grid voltage and background pressure were held constant at -500 V and 8.3×10^{-6} Torr, respectively. Then tests were conducted at various background pressures while beam current and accel-grid voltage were held constant at 2.0 mA and -500 V, respectively.

Finally, beam current was maintained at 2.0 mA and background pressure was held at 8.3×10^{-6} Torr while tests were conducted at different accel-grid voltages.

The continual impingement of charge-exchange ions on the downstream side of the accel grid during a test, induced sputter erosion of the multi-layer coating and yields patterns similar to that shown in Fig. 8. The particular pattern shown was observed after operation at screen (V_+) and accel-grid (V_-) voltages of +1000 V and -300 V, respectively, and cathode and neutralizer flow rates each at 46 mA equivalent xenon (0.5 sccm). These operating conditions were maintained for t=~270 minutes at an average impingement current (J_i) of 47 μA measured at a beam current of 2.0 mA. This particular figure shows erosion patterns on the 19-hole grid set between accel-grid apertures (i.e. pits and trench) and outside accel-grid apertures (periphery). Lighter areas in Fig. 8 correspond to copper layers, and darker areas to stainless steel. The white circles of Fig. 8 are the accel-grid apertures. The first interface between alternating stainless steel and copper layers can be seen in the periphery area, outside the active beam area. Layer interfaces are seen to be much closer together near the center of the grid than they are in the periphery region, suggesting that sharper erosion and impingement current gradients exist near the center of the grid.

A more detailed photograph of two pits and the trench between them is shown in Fig. 9 along with operating conditions. Again, darker and lighter areas correspond to stainless steel and copper layers, respectively. In this case, however, a different photographic technique was used and the apertures are shown as dark black semicircular areas. The erosion pattern centered between the center and two ring #1

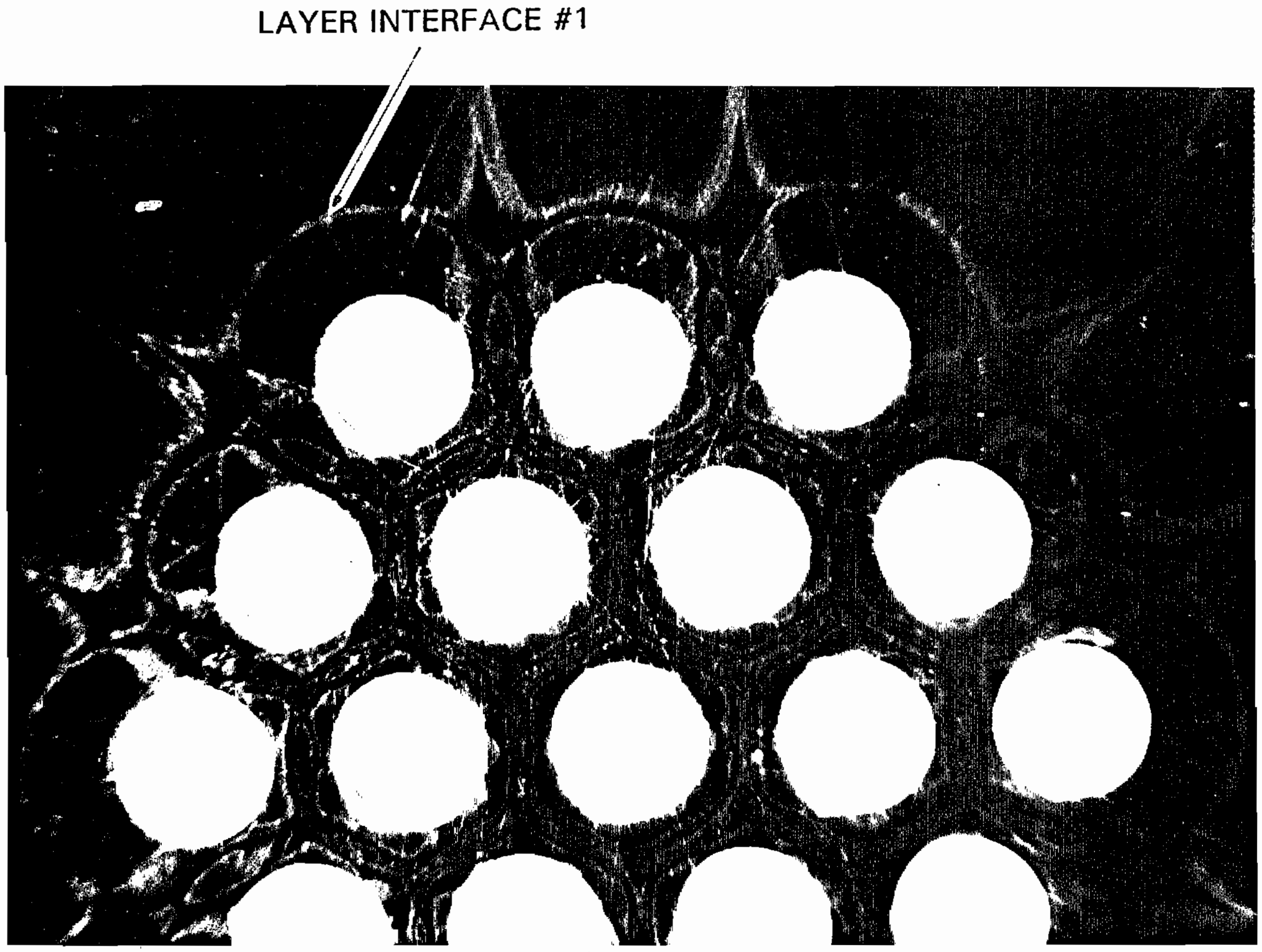

$V_+ = +1000$ V
$V_- = -300$ V
$J_B = 2.0$ mA
$J_i = 47$ μA
$\dot{m} = 46$ mA eq. (Xe)
$P_o = 8.3 \times 10^{-6}$ Torr
$t = 270$ min

Fig. 8 Typical Erosion Patterns

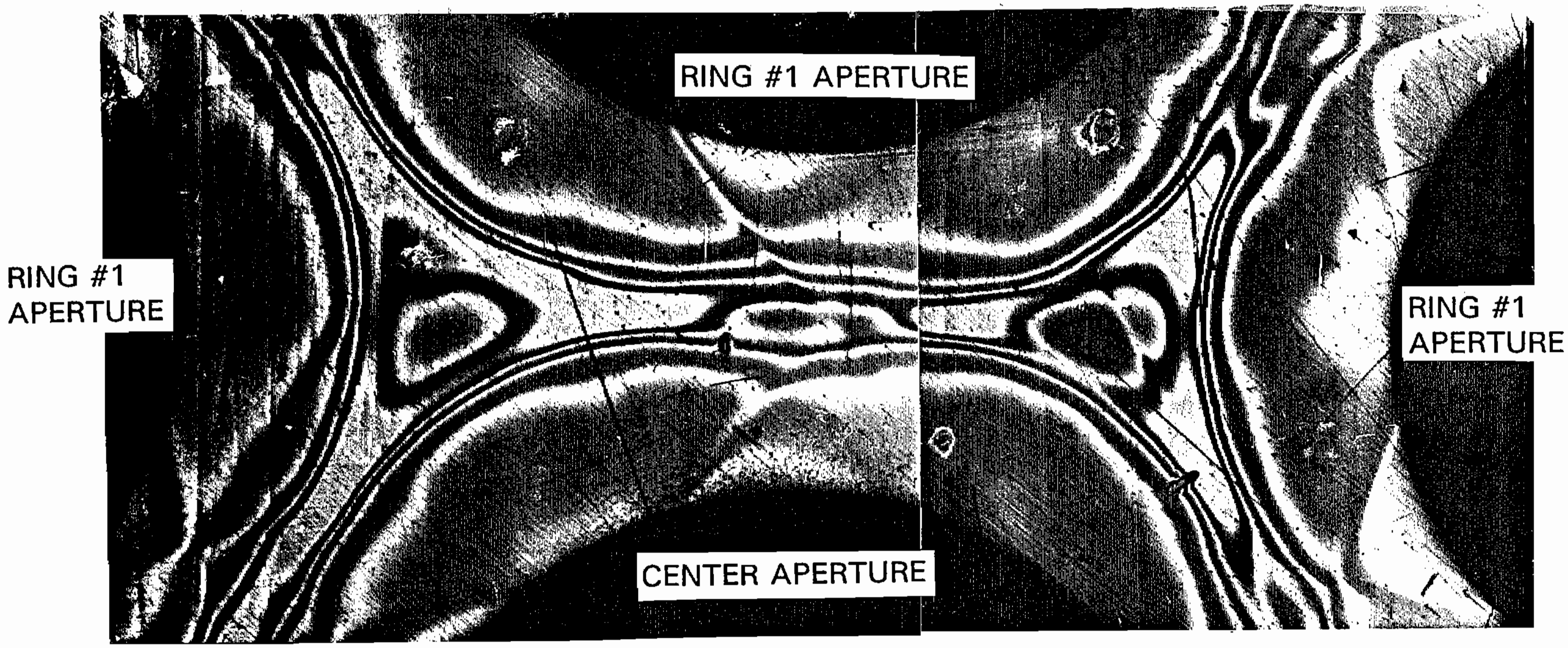

$V_+ = +1000$ V
$V_- = -300$ V
$J_B = 2.0$ mA
$J_i = 47\ \mu A$
$\dot{m} = 46$ mA eq. (Xe)
$P_o = 8.3 \times 10^{-6}$ Torr
$t = 270$ min

Fig. 9 Typical Detail of Pit and Trench Erosion apertures (pit), is often quite complex. For example, Fig. 10a shows a complex pit erosion pattern obtained from a grid set operated for approximately 210 minutes at the operating conditions indicated on the figure. Because some of the interfaces between layers close on themselves (e.g. layer interface A), it is impossible to determine whether a layer is higher or lower than an adjacent one in some cases. In order to identify layer numbers accurately the diagnostic-etch technique developed at Hughes Research Labs [12] was applied. This technique involved the placement of a graphite mask ~1.6 mm above an erosion-patterned surface and subsequent sputter erosion of the sample to the base surface using an argon ion beam similar to that used for sputter coating. An example of a grid region which was subjected to the diagnostic etch procedure to establish particular layer numbers is shown in Fig. 10b. The grid erosion pattern of Fig 10a is etched until all layers have been eroded and the base is visible on one region of it. One can then identify layer 12 and generally the other layers (layer 1 is on top and layer 12 adjacent to the accel-grid SS substrate). Diagnostic etches were used as necessary to establish layer numbers when their identities were uncertain.

B. Analysis and Interpretation

Although the testing of coated accel grids is useful for establishing ion-impingement erosion patterns, ion thruster grid sets are typically constructed from molybdenum rather than copper and stainless steel. In order to make the erosion-pattern results being measured in this study applicable to actual thrusters, measured depth-erosion and volumetric-erosion rates were converted to equivalent molybdenum-erosion rates.

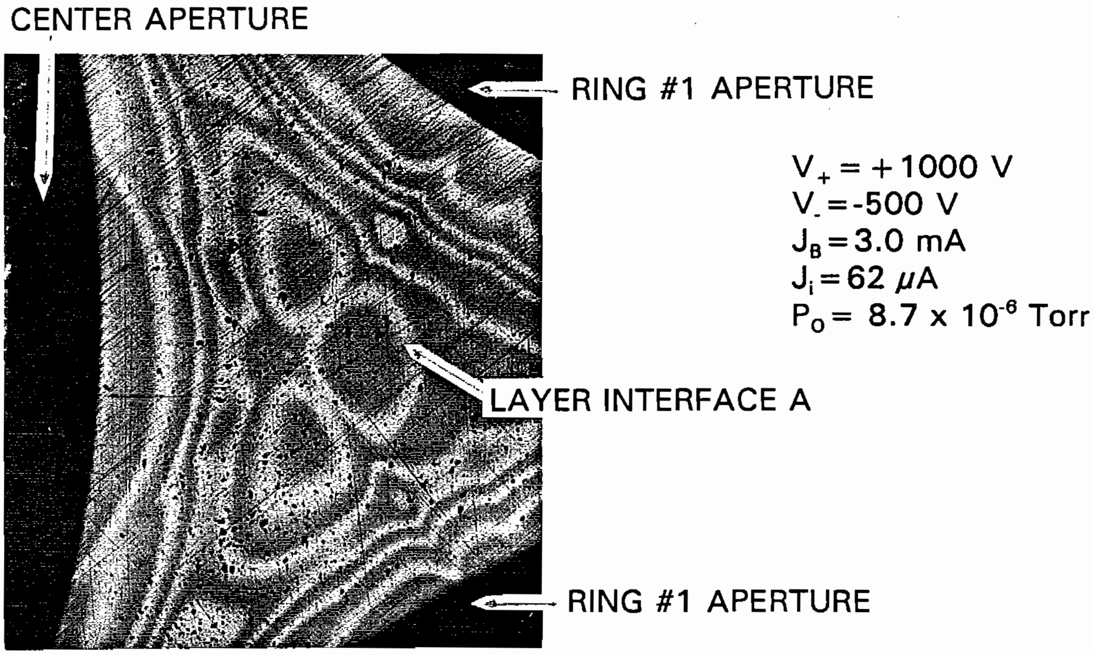

a. Erosion Pattern After Thruster Operation

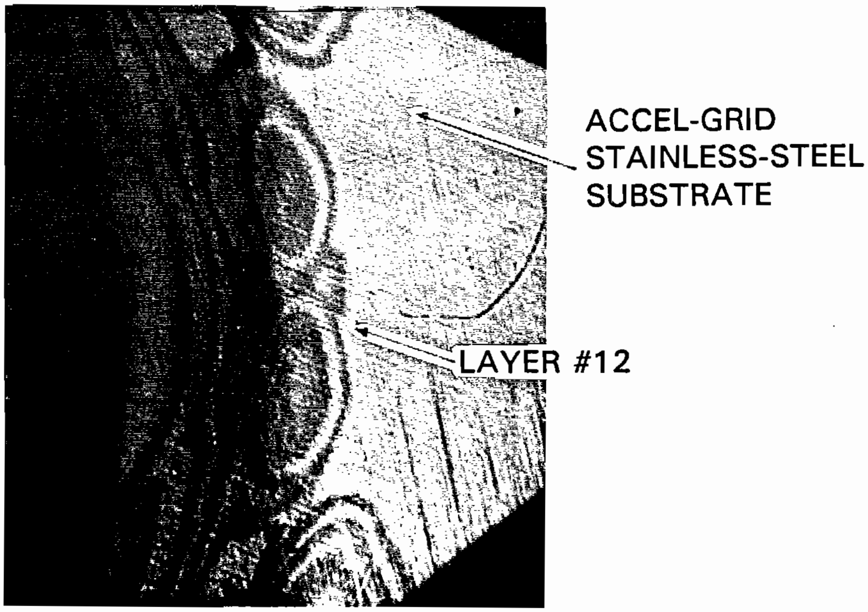

b. Erosion Pattern After Diagnostic Etch

Fig. 10 Typical Erosion-Pattern Data from an Accel-Grid Test

The methodology used to achieve this conversion is described in the following paragraphs.

Figure 11a shows a layer identification map of one of the pit-erosion areas of Fig. 9, along with the corresponding operating conditions. Several stainless steel and copper layer numbers are labeled (1 on top, and 12 next to the stainless-steel substrate); they are consistent with diagnostic-etch results. Assuming uniform material properties and constant impingement current densities, the time it takes to erode to any layer interface shown in Fig. 11a is the time of the test (t). For example, at point A shown in the figure, the accel grid was subjected to a specific impingement current density (j_i) for a total of 270 minutes and five copper layers and five stainless steel layers were eroded off. This test time (t=270 minutes) is then, the sum of times it took to erode through five individual copper layers (t_{Cu}) and five of the individual stainless steel layers (t_{SS}). The amount of time it takes to erode through all five, 500 Å copper layers (x_{Cu}=2500 Å) is given by

$$t_{Cu} = \frac{x_{Cu}\, e\, \rho_{Cu}}{j_i\, S(\epsilon)_{Cu}\, m_{Cu}} , \tag{7}$$

where, again, ρ_{Cu}, $S(\epsilon)_{Cu}$, and m_{Cu} are the density, sputter yield*, and atom mass, respectively, of the sputtered copper. Similarly, the time to erode through five, 500 Å layers (x_{SS}=2500 Å) of stainless steel is given by

---

It is noted that the phenomenon called texturing [16] can alter the sputter yield of one material when it is contaminated by another. Microscopic examination of sputter eroded surfaces showed no evidence of texturing in these tests.

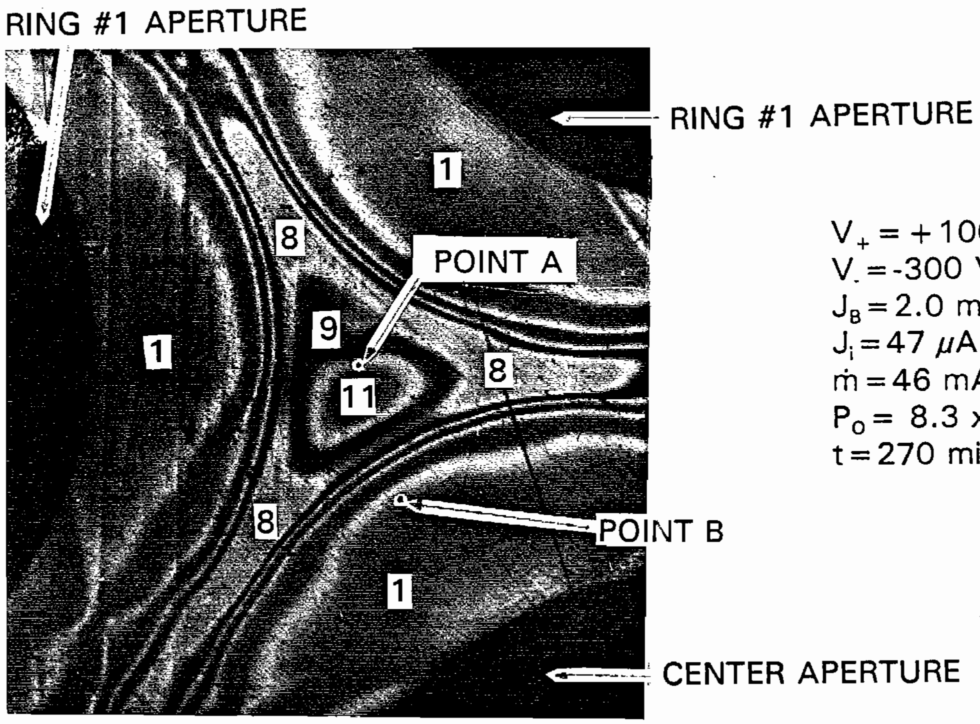

$V_+ = +1000$ V
$V_- = -300$ V
$J_B = 2.0$ mA
$J_i = 47\ \mu$A
$\dot{m} = 46$ mA eq. (Xe)
$P_0 = 8.3 \times 10^{-6}$ Torr
$t = 270$ min

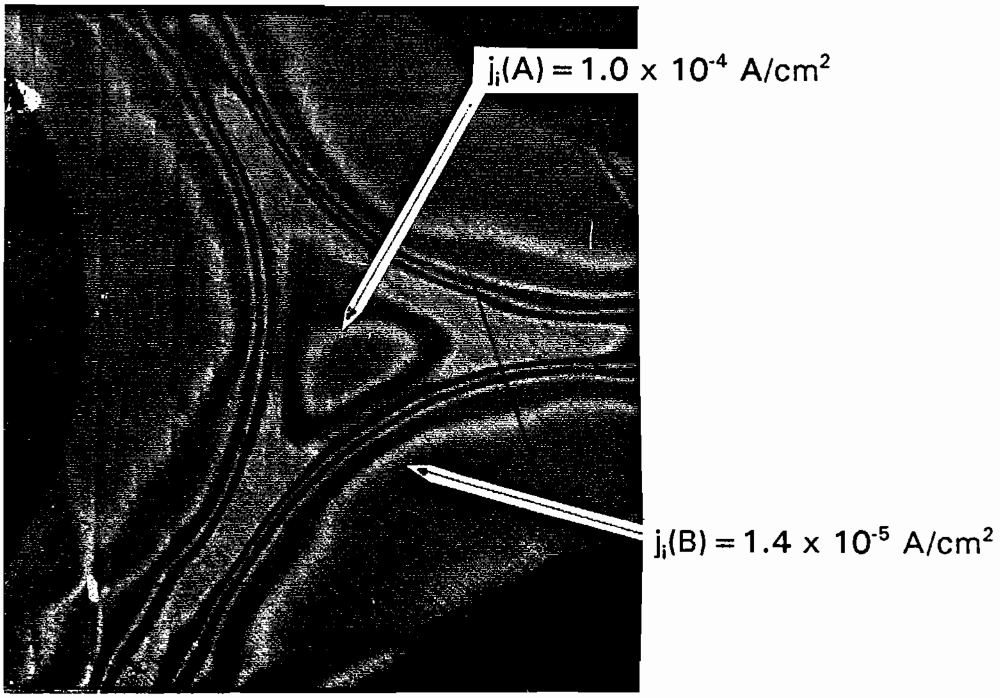

b. Corresponding Impingement-Current-Density Contours

Fig. 11 Accel-Grid Erosion Map

$$t_{SS} = \frac{x_{SS}\, e\, \rho_{SS}}{j_i\, S(\epsilon)_{SS}\, m_{SS}} \; . \tag{8}$$

Hence the total time to erode through x_{Cu} and x_{SS} is

$$t = \frac{e}{j_i}\left(\frac{x_{Cu}\,\rho_{Cu}}{S(\epsilon)_{Cu}\, m_{Cu}} + \frac{x_{SS}\,\rho_{SS}}{S(\epsilon)_{SS}\, m_{SS}} \right) \; . \tag{9}$$

Since the time (t) in Eq. 9 is known (the test time ~270 min.), and the copper and stainless steel thicknesses x_{Cu} and x_{SS} are known (each at 2500 Å), the current density (j_i) at point A can be determined. In a similar manner, one can solve for the impingement current density at any location where the erosion depth is known (i.e. at the layer interfaces) using Eq. 9. For example, applying Eq. 9 to the layer interface at point A and point B of Fig. 11a, impingement-current densities shown at these points on Fig. 11b are obtained. As expected, the highest impingement current densities are seen in the center of the pits where the erosion is the deepest. Knowing the current densities along each of the alternating layer interfaces, the corresponding thicknesses of molybdenum (x_{Mo}) that would be eroded in time t or the ratio of these (i.e. the depth-erosion rate) for molybdenum along an interface can be determined. This molybdenum depth-erosion rate is obtained using Eq. 10, which is similar to Eqs. 7 and 8, but with corresponding molybdenum values.

$$\frac{x_{Mo}}{t} = \frac{m_{Mo}\, S_{Mo}(\epsilon)\, j_i}{e\, \rho_{Mo}} \tag{10}$$

The molybdenum depth-erosion rate profiles computed using Eq. 10 and the erosion pattern data of Fig. 9 along the straight line path between A-A$'$ (i.e. along a trench) and for path B-B$'$ (i.e. across a trench) are shown in Fig. 12. The shaded areas on either side of the depth-erosion rate profile represent the accel-grid apertures. The data presented in Fig. 12a show that an equivalent molybdenum pit erosion rate of 0.21 μm/hour would be found operating at the conditions indicated in the legend. Likewise, both Figs. 12a and 12b indicate an equivalent trench erosion rate of 0.13 μm/hour. On both depth-erosion rate profiles, a single error bar is shown. This error bar can be applied to all of the depth-erosion rates (open circles) and is due to uncertainties in the parameters of Eq. 9 used to calculate the impingement current density used in Eq. 10. In particular, the copper and stainless steel coating thicknesses and sputter yields were only known to within ~3% and ~6% respectively. Thus, the depth-erosion rates shown in Fig. 12 are only known to within ~10%, assuming that the molybdenum sputter yield is known. Sputter yield values used for molybdenum, sputtered stainless steel and copper are shown in Table 1B of Appendix B. Effects of beam current, background pressure, and accel-grid voltage on depth-erosion rate profiles like those presented in Fig. 12 will be examined, as will changes in pit and trench shapes induced by changes in operating conditions and the impingement-current-density distributions they induce.

Pit and trench shapes, represented through the use of a shape factor (S_f), were examined by modeling the pits as inverted right circular cone frustra and trenches as trapezoidal in cross section. Figure 13 shows the erosion-depth rate profiles of Fig. 9 overlaid with the cross-sectional elements used to model the profiles (described in the previous chapter and Appendix A). Specifically, shown in Fig. 13a is a labeled cone

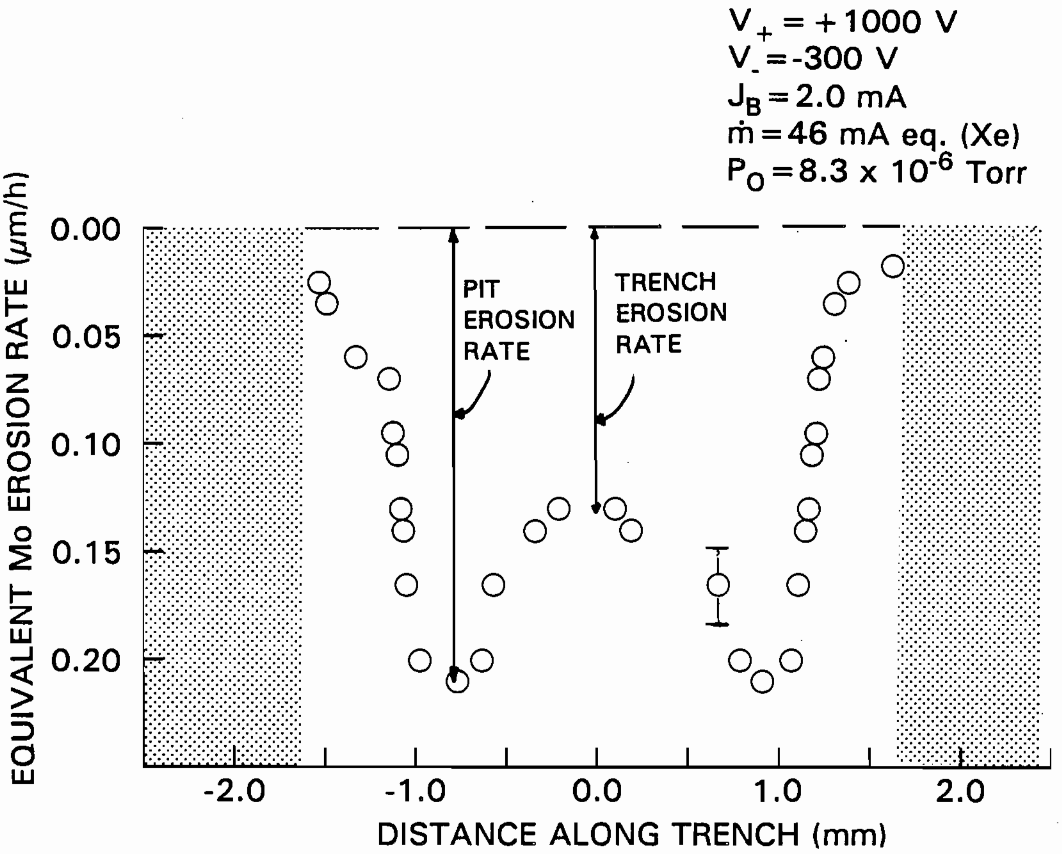

a. Across Two Pits and Along Trench (Section A - A′ of Fig. 4)

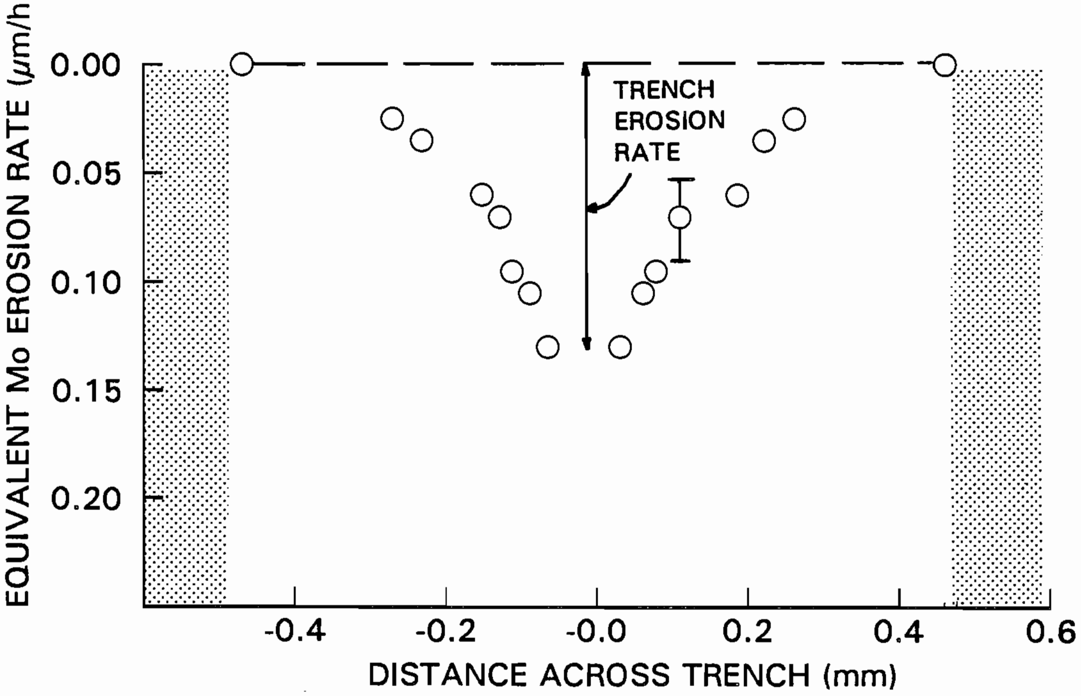

b. Across Trench at Its Midpoint (Section B - B′ of Fig. 4)

Fig. 12 Typical Erosion Rate Profiles

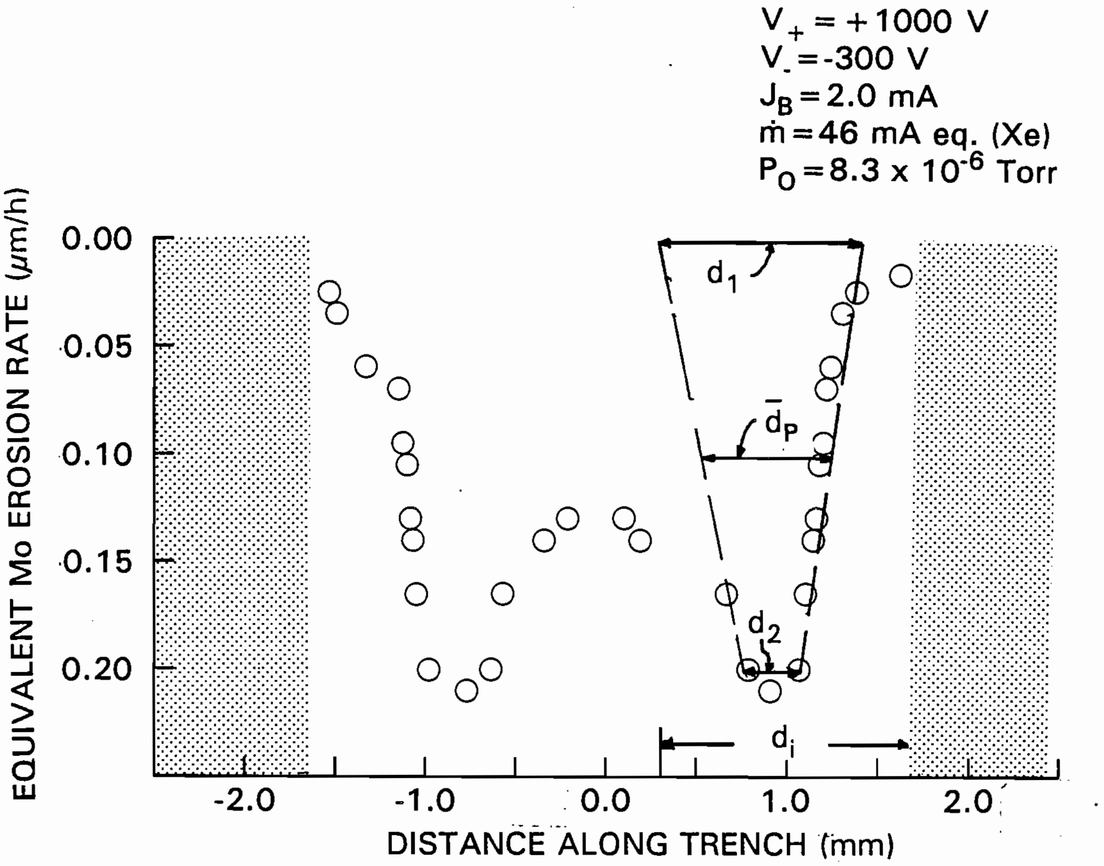

a. Idealized Pit Parameters

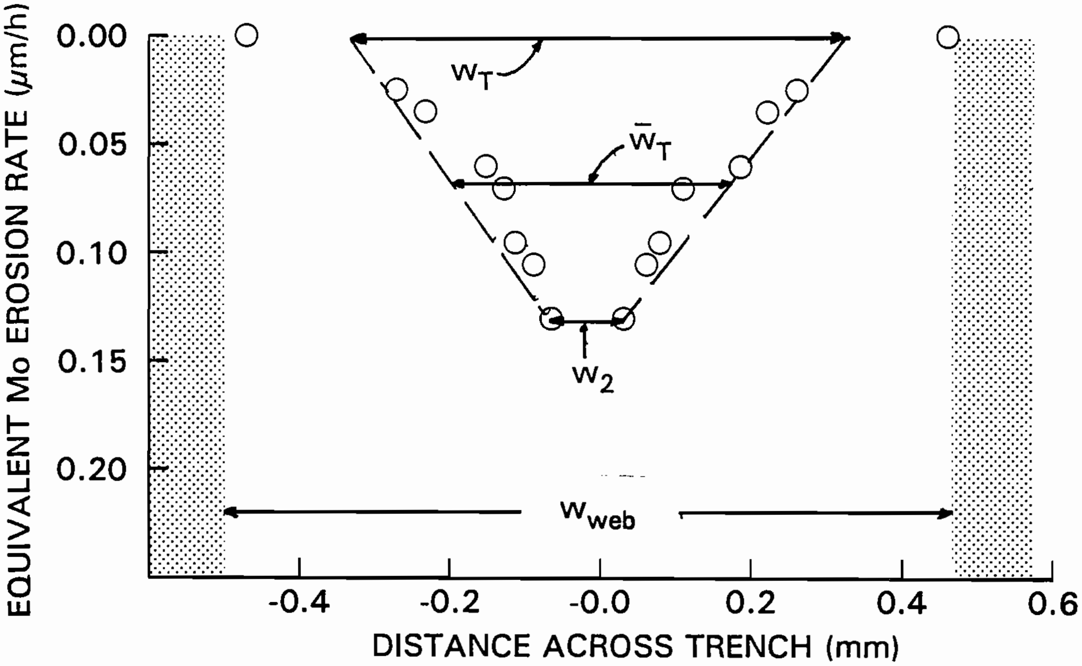

b. Idealized Trench Parameters

Fig. 13 Erosion Shape Parameter Definitions frustrum overlaid on the erosion-rate pit-profile data. This frustrum with diameter d_2 at the pit base and d_1 at the original surface of the grid has a mean depth diameter (full diameter at the half-erosion-rate level) d_p. The other symbol (d_i) on the figure is the diameter of the circle that can be inscribed tangent to three adjacent apertures. The shape factor selected for pits is the ratio d_p/d_i. For the case of Fig. 13, it has a value of 0.53. As impingement-current-density distribution becomes more uniform, this pit shape factor would increase and approach unity, and as the distribution becomes more highly focussed into the center of the pit, the factor would decrease toward zero.

Figure 13b shows the trench erosion rate profile with the cross sectional trapezoidal model and its dimensions overlaid. Trench shape factors are calculated in a manner consistent with that for the pits by dividing the full width of the trapezoid at the mean trench erosion rate ($\bar{w}_T$) by the maximum possible trench width (W_{web}). This maximum trench width is the minimum width of the accel grid webbing between two adjacent apertures. As shown in Fig. 12, $\bar{w}_T=(w_T+w_2)/2$ is the mean width of the trench. The shape factor for the trench as shown in Fig. 13 has the value of 0.37 and it can also range from unity for a uniform impingement-current-density distribution to zero for a highly peaked one.

Pit and trench erosion rates will be used in conjunction with pit and trench shape and impingement current density uniformity factors to describe the effect of changes in thruster operating parameter effects on accel-grid erosion characteristics. It is important to note, however, that these depth-erosion rates and shape current density uniformity factors within the pit and trench regions are only valid assuming that the impingement-current-density distribution is constant throughout the life of the accel-grid. In reality, as the erosion becomes deeper on the accel-grid, the equi-potential lines just downstream of the accel grid begin to change. This change in the equi-potential lines influences the trajectories of the charge-exchange ions which are impinging on the accel-grid. Therefore the impingement-current-density distribution is not constant throughout the life of the accel-grid. Consequently, the accel-grid depth-erosion rates and shape/current density uniformity factors give a better indication of initial erosion characteristics than of end-of-life ones.

IV. Experimental Results

A. Effect of Operating Parameters on Impingement Current

The effects of changes in beam current, background pressure, and accelerator grid potential on accel-grid erosion characteristics for two-grid sets have been investigated. These thruster operating parameters were selected for study because they were identified as ones that should have a dominant influence on the sputter-erosion behavior of an accel grid. Accel-grid erosion characteristics will be shown over a wide range of these operating parameters. Since the sputter erosion rate on the downstream side of an accel grid is directly proportional to impingement current, however, it is appropriate to first consider the effect of each of these parameters on impingement current. Figure 14 shows the effect of beam current on impingement current. It indicates measured accel-grid impingement current (open circles) increases linearly from ~zero to 100 μA as beam current is varied from zero to ~3.5 mA. This is expected because the charge-exchange-ion production rate is directly proportional to beam current [11]. Increasing beam current above ~3.5 mA, causes primary beam ions to begin striking the accel grid (direct impingement), and this causes the greater-than-linear increase in the measured impingement current at the highest beam current data point in Fig. 14. If the distribution of ions impinging on the grids were unaffected by increases in beam current, one would also expect to see depth-erosion rates (given by

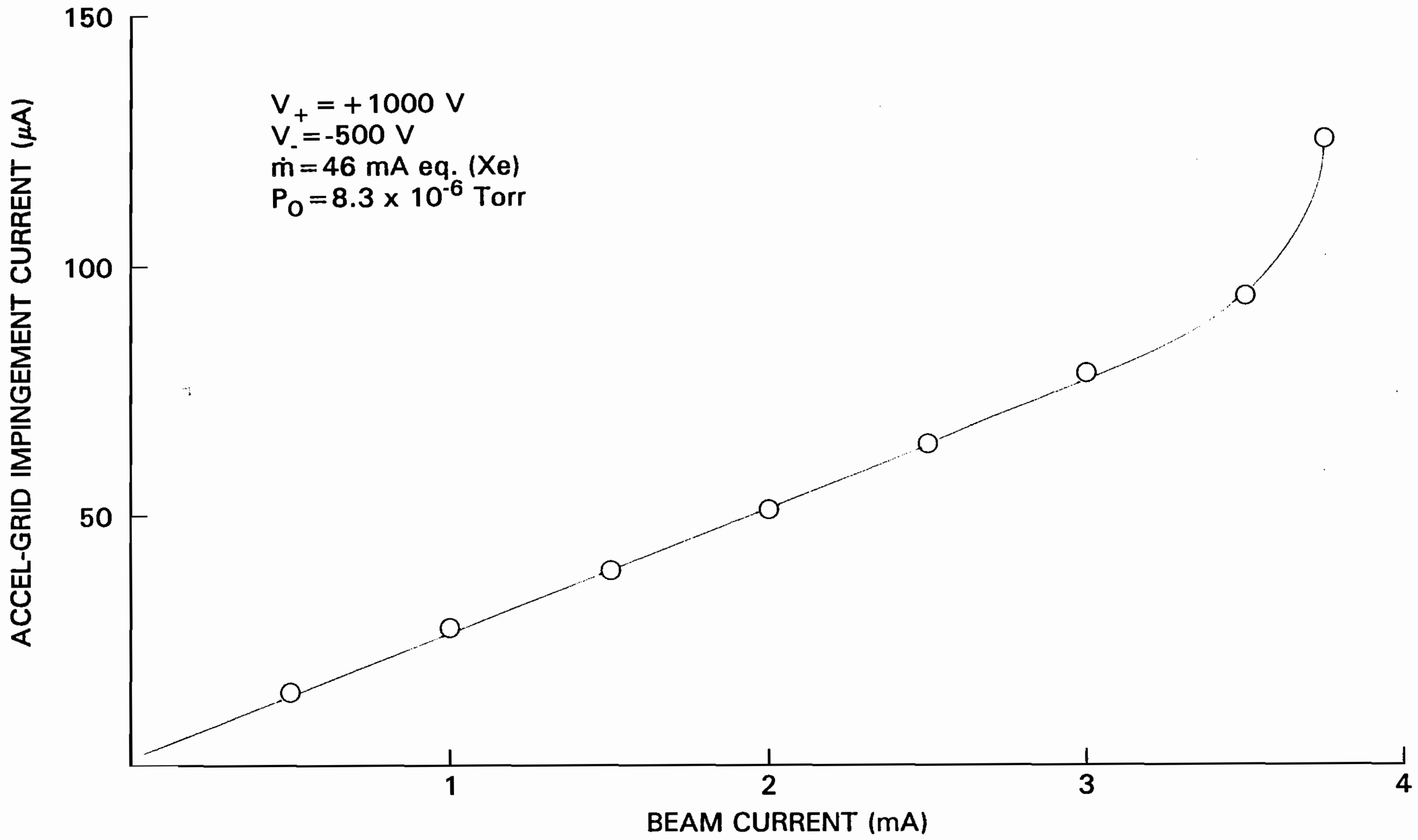

Fig. 14 Effect of Beam Current on Accel-Grid Impingement Current

Eq. 2) to increase linearly with impingement current up to the point of inception of direct impingement.

The effects of background pressure on impingement current are presented in Fig. 15a. This figure shows that impingement current increases linearly from ~50 μA to ~85 μA as background pressure is increased from a nominal value of 8.3 x 10^{-6} Torr up to 4.0 x 10^{-5} Torr. This is expected because greater neutral propellant atom densities downstream of the accel grid, yield a greater charge-exchange collision rate and thus, greater impingement currents. These higher impingement currents might be expected to induce proportional increases in the total volumetric erosion rate. Again, depth-erosion rates should be directly proportional to volumetric erosion rates provided changes in pressure do not change the factors that describe the distribution of the impinging ions across the grids (i.e. the impingement current density uniformity factor (f) and active beam to peripheral impingement current distribution factor (δ)).

Impingement currents measured as the accel-grid potential magnitude was increased from -100 to -900 V are given in Fig. 15b along with the thruster operating conditions that were held constant. From this figure, it is evident that impingement current increases linearly from ~40 μA to ~60 μA as accel-grid voltage magnitude is increases. Monheiser has shown that the size of the near-field charge-exchange ion-production region increases with accel-grid voltage magnitude. This induces a proportional increase in impingement current. Sputter yield also increases with accel-grid voltage magnitudes (see Appendix B). Hence sputtering rate, which is proportional to the product of impingement current and sputter yield, increases with

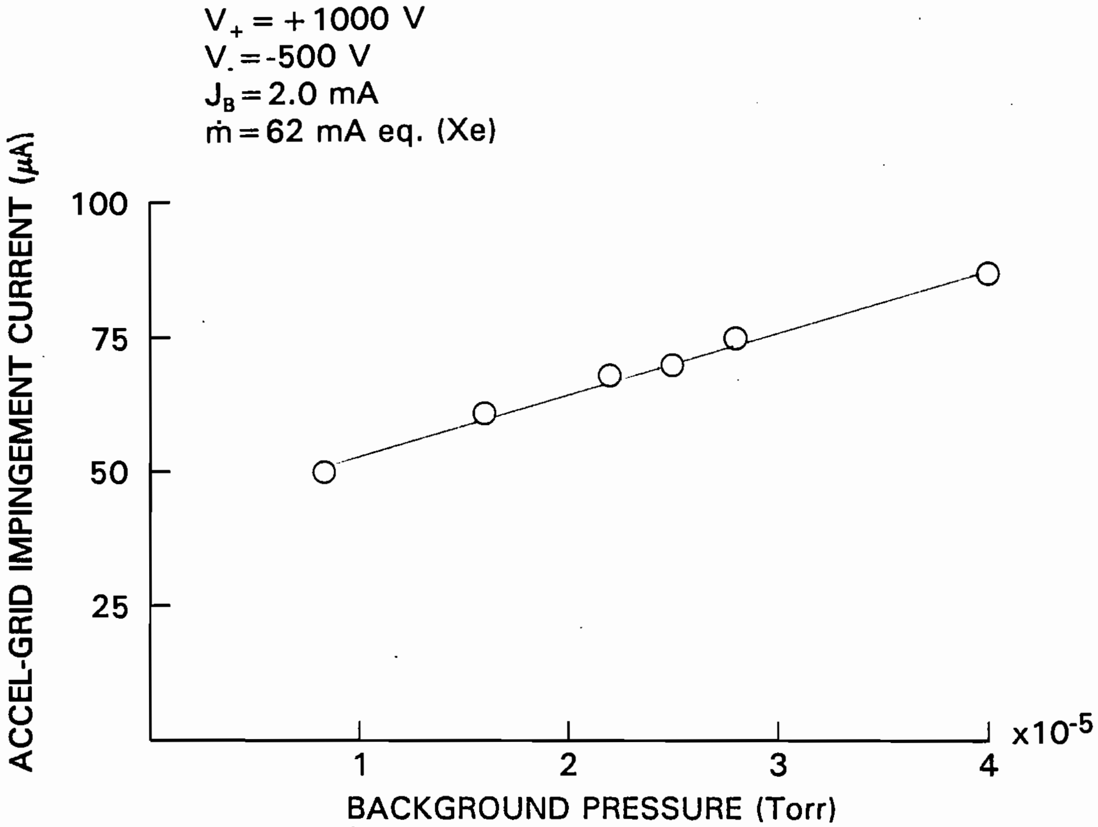

a. Effect of Background Pressure

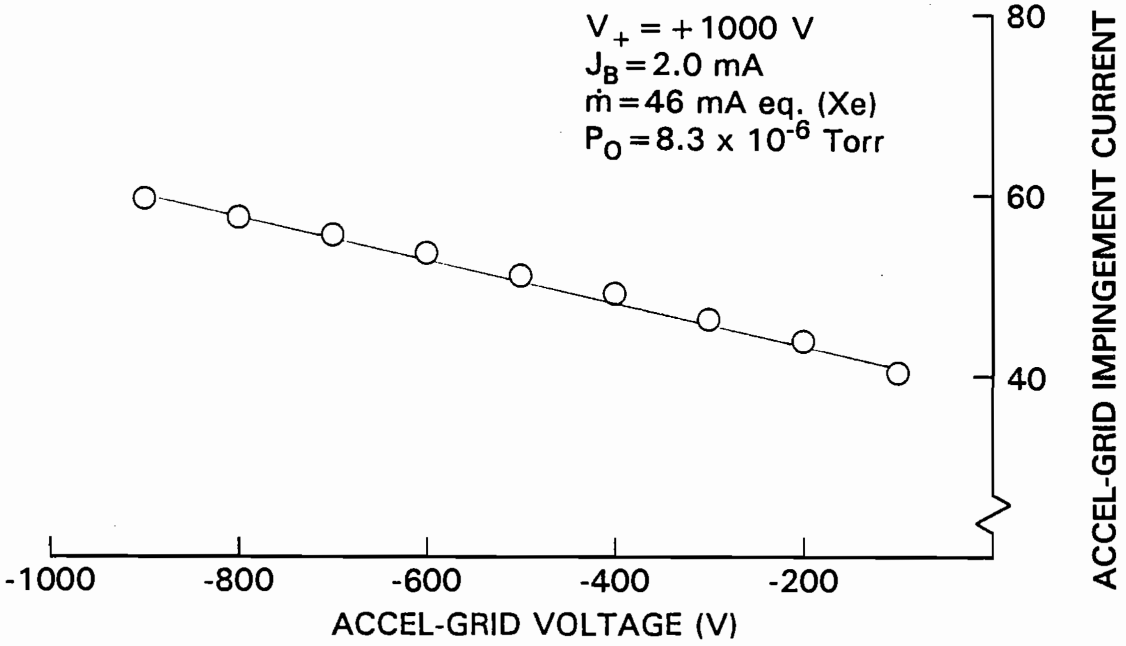

b. Effect of Accel-Grid Voltage

Fig. 15 Effect of Operating Conditions on Accel-Grid Impingement Current accel-grid voltage magnitude.

B. Effect of Operating Parameters on Erosion Rates.

Molybdenum depth-erosion rates measured from multilayer erosion monitors at three different beam currents are shown in Fig. 16a for both pits (open circles) and trenches (open squares) at the thruster operating conditions indicated in the figure. These data suggest 1) depth-erosion rates for pits and trenches are directly proportional to beam current and 2) pit depth-erosion rate increases more rapidly with beam current than trench depth-erosion rate. Equivalent molybdenum volumetric-erosion rates based on all experimental measurements (pit+trench+periphery) are compared to equivalent theoretical values determined from impingement currents (using Eq. 5) in Fig. 16b. Both erosion rates increase linearly up to a beam current of ~3.0 mA, as expected from the impingement current plot of Fig. 14, and are in agreement to within ~10%. At a beam current of 3.75 mA, however, the experimental erosion rate is significantly less than the corresponding theoretical rate. This lower experimental erosion rate is expected because: 1) some of the ions contributing to the impingement current strike the accel grid where erosion is not measured by the multilayer erosion technique (e.g. the interior surface or barrel of the accel-grid aperture), and 2) the cross sections of the pits and trenches are not modeled well by the shapes being used to represent them. Thus, experimental erosion rates are underestimated when direct impingement is occurring.

The ratio of pit and trench depth-erosion rates to the total volumetric erosion rates are shown in the erosion proportionality plot of Fig. 17a. Recall that the erosion

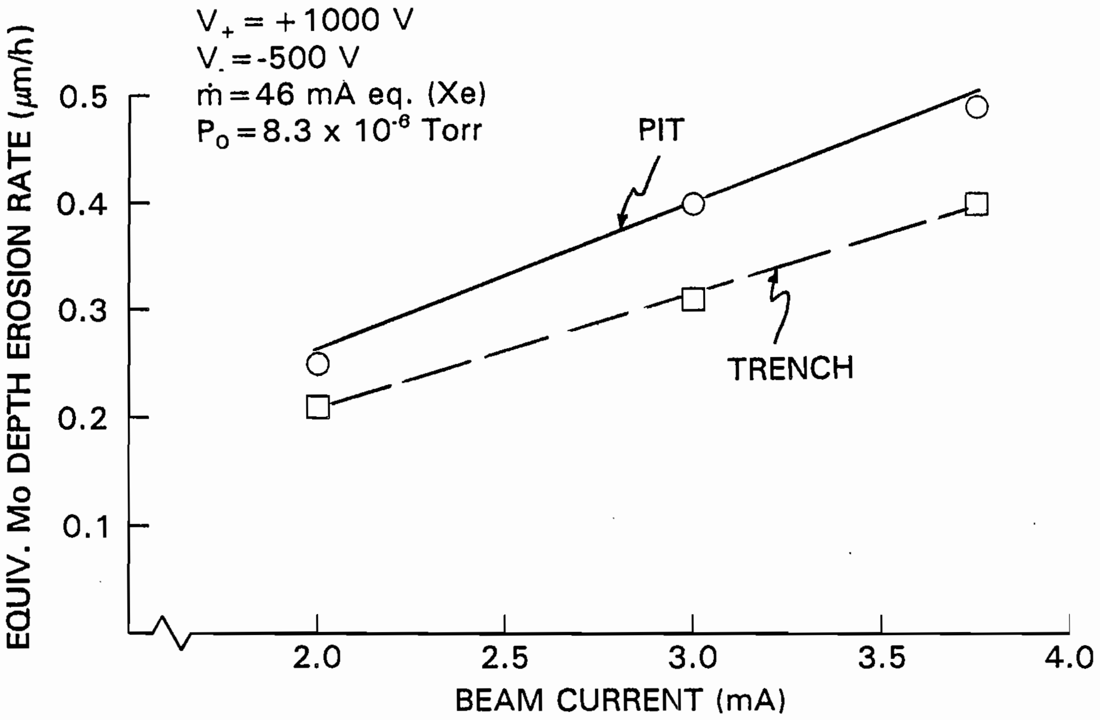

a. Pit and Trench Depth-Erosion Rates

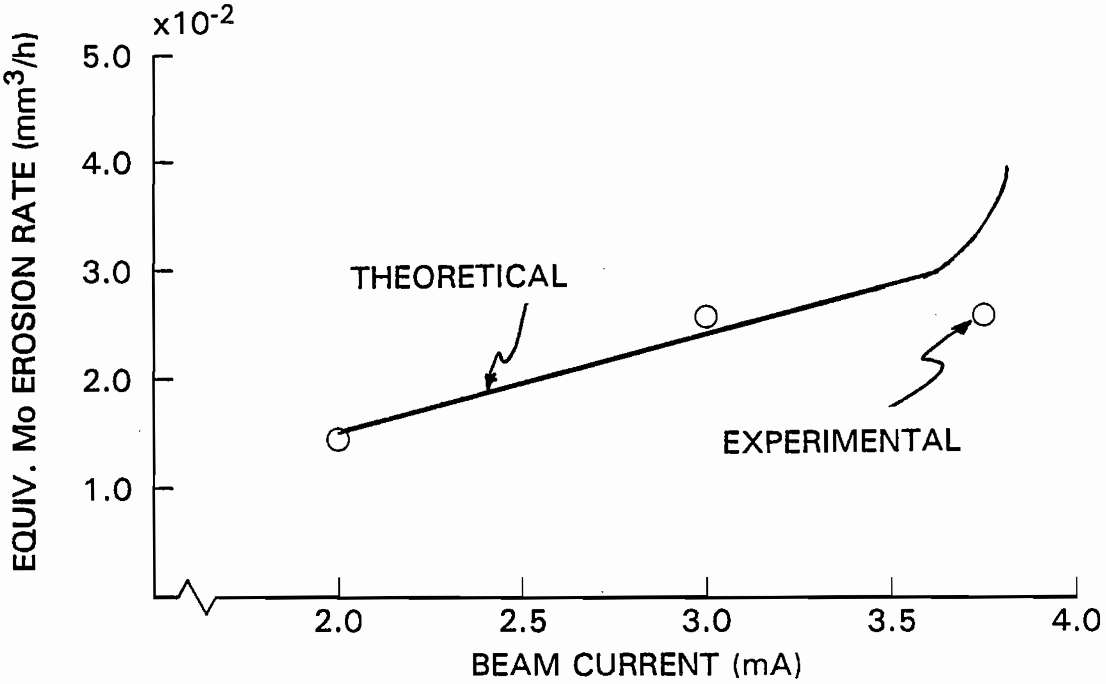

b. Experimental and Theoretical Volumetric-Erosion Rates

Fig. 16 Effect of Beam Current on Equivalent Molybdenum Erosion Rates

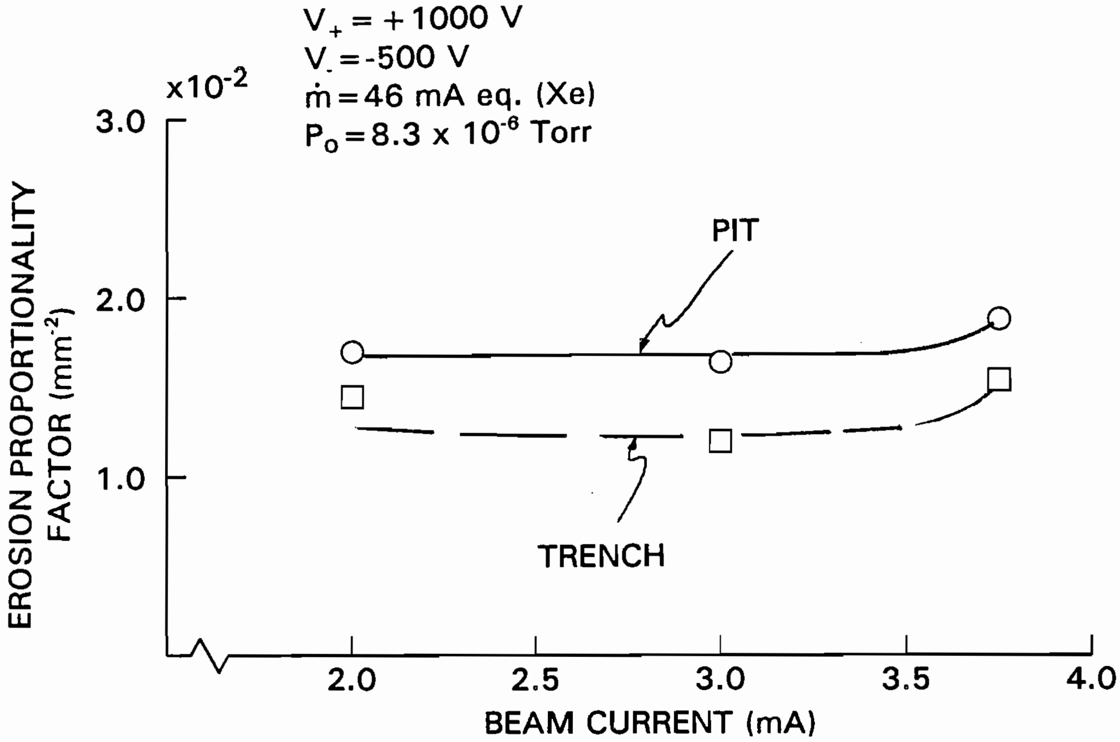

a. Pit and Trench Proportionality Factors

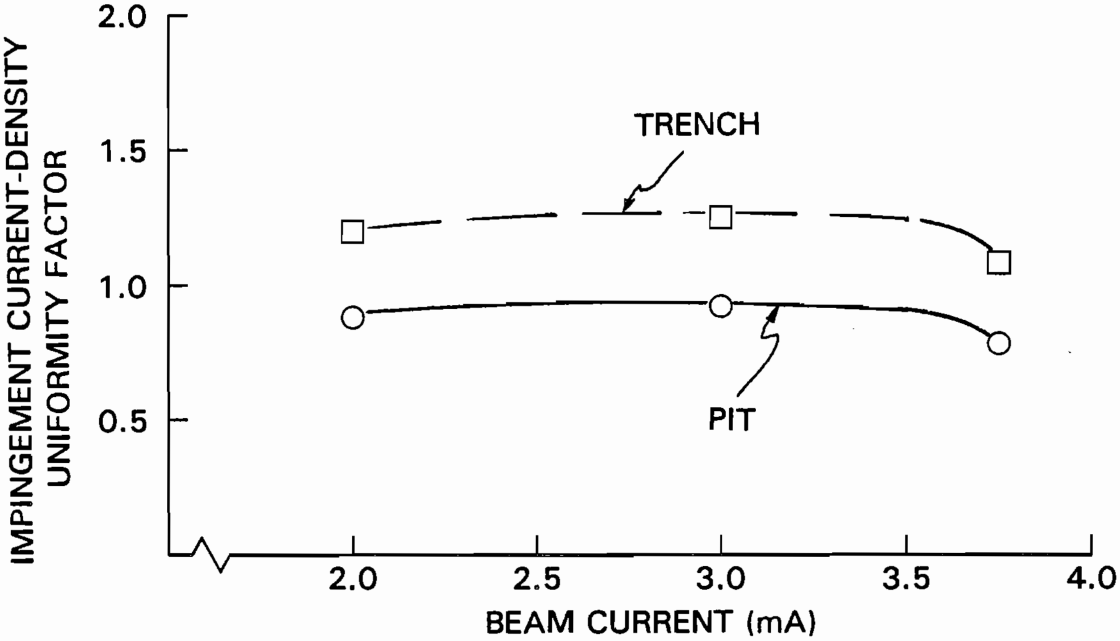

b. Pit and Trench Impingement Current-Density Uniformity Factors

Fig. 17 Effect of Beam Current on Accel-Grid Erosion proportionality factors (P) plotted in Fig. 17a are found by dividing the experimental depth-erosion rates (Fig. 16a) by the total volumetric-erosion rates (open circles in Fig. 16b). The relatively minor changes in the pit and trench erosion proportionality factor suggest that both the depth and volumetric-erosion rates increase in almost direct proportion. The slight increase in the proportionality factors at the higher beam current of 3.75 mA is caused by accel-grid operation with direct impingement and is not of concern at normal thruster operating conditions. Again, direct ion-impingement current on the accel-grid leads to an underestimation of the total volumetric-erosion rate found using this particular erosion measuring technique.

The impingement current density uniformity factors (f values within Eq. 2) for the pits and trenches are shown in Fig. 17b. Data for the pit show impingement current density uniformity varies only slightly over the entire range of which beam current variation. The trench impingement current density uniformity factor follows the same trend as the pit. Above a beam current of 3.75 mA, however, both depart from the expected linear trend because the accel-grid is under direct impingement. It is noted that the periphery erosion factor (δ) remained nearly constant at ~4% as beam current was varied over the full range.

How the shapes of the pits and trenches vary with beam current can be seen from the shape factor plot shown in Fig. 18. Pit shape factor is shown to vary between 0.6 and 0.7 over the entire beam current range. Trench shape factor appears to increase gradually with beam current up to ~3.5 mA and then to rapidly rise to 1.0 at a beam current of 3.75 mA where direct impingement was observed. Ions which are

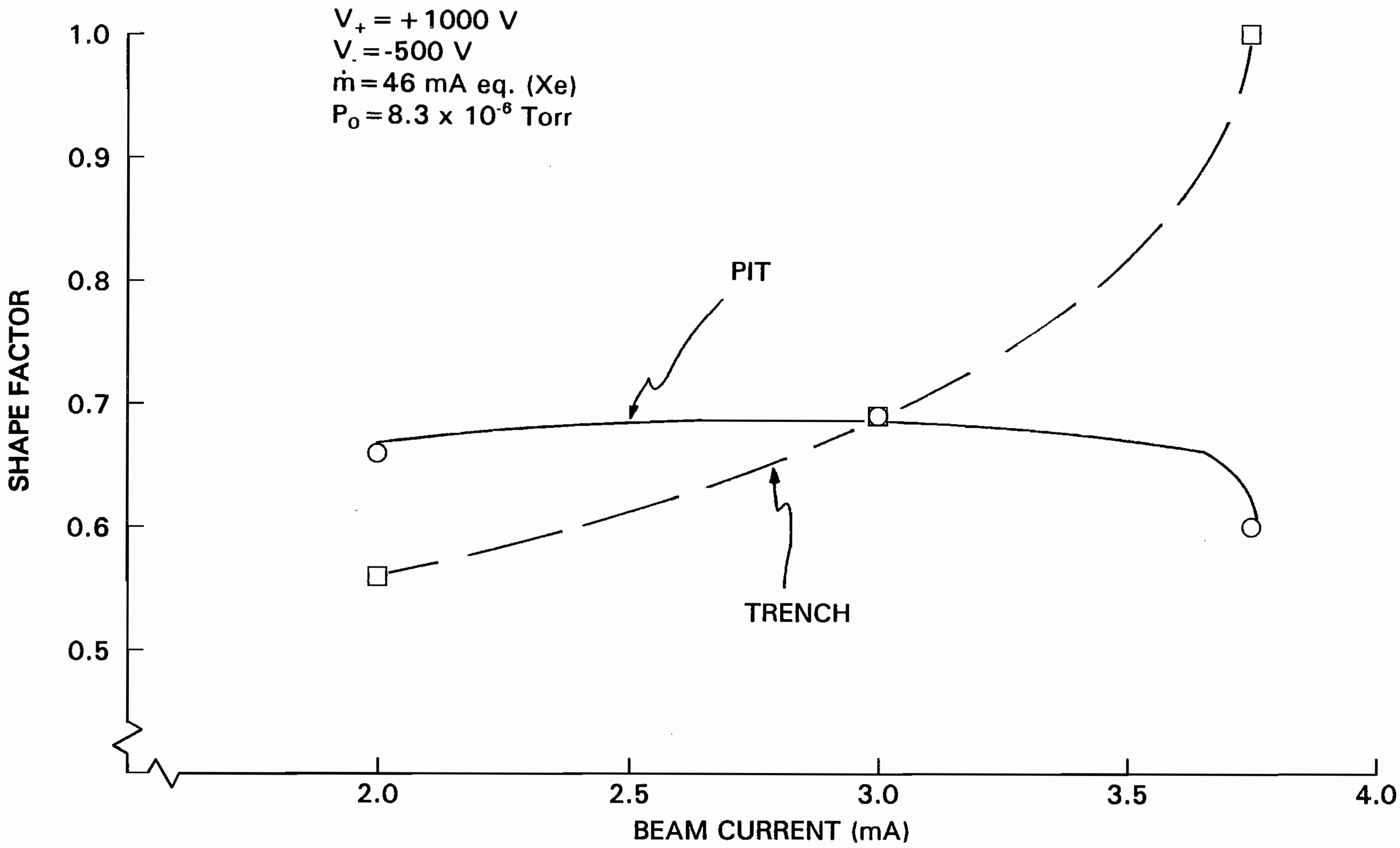

Fig. 18 Effect of Beam Current on Pit and Trench Shape Factors

striking the barrel of the accel-grid lead to severe erosion on the downstream periphery of the aperture, thereby producing erosion which tends to remove the mesa. This effect can be clearly seen from the depth-erosion profiles overlaid with the cross-sectional erosion model elements in Fig. 19. In particular, the erosion profiles along a trench between two pits (Fig. 19a) and across a trench (Fig. 19b) show that the erosion depths at the hole edges are greater than those in the pits or trenches. For this special erosion case, it is important to note that the basic shapes of the eroded volumes (frustrum of cone for a pit and a trench with trapezoidal cross section) do not describe the observed erosion. Furthermore, it is noted that the erosion patterns shown in Fig. 19 suggest the impingement current density distribution is altered near the onset of direct impingement, so it becomes more uniform across the webbing.

These data have shown that pit and trench depth-erosion rates increase linearly with beam current. These depth-erosion rates are directly proportional to the volumetric-erosion rates to the extent that the pit and trench impingement current density uniformity factors remain relatively constant with beam current. Since the relative distribution of impingement current between the active and peripheral regions remains almost constant as beam current is varied, the proportionality factor results suggest that initial pit and trench depth-erosion rates can be computed with good accuracy from the total volume of erosion-rate measurements.

Molybdenum depth-erosion rates (open circles for pits, open squares for trenches) measured as a function of background pressure are plotted in Fig. 20a. Both pit and trench depth-erosion rates decrease linearly as pressure is increased to

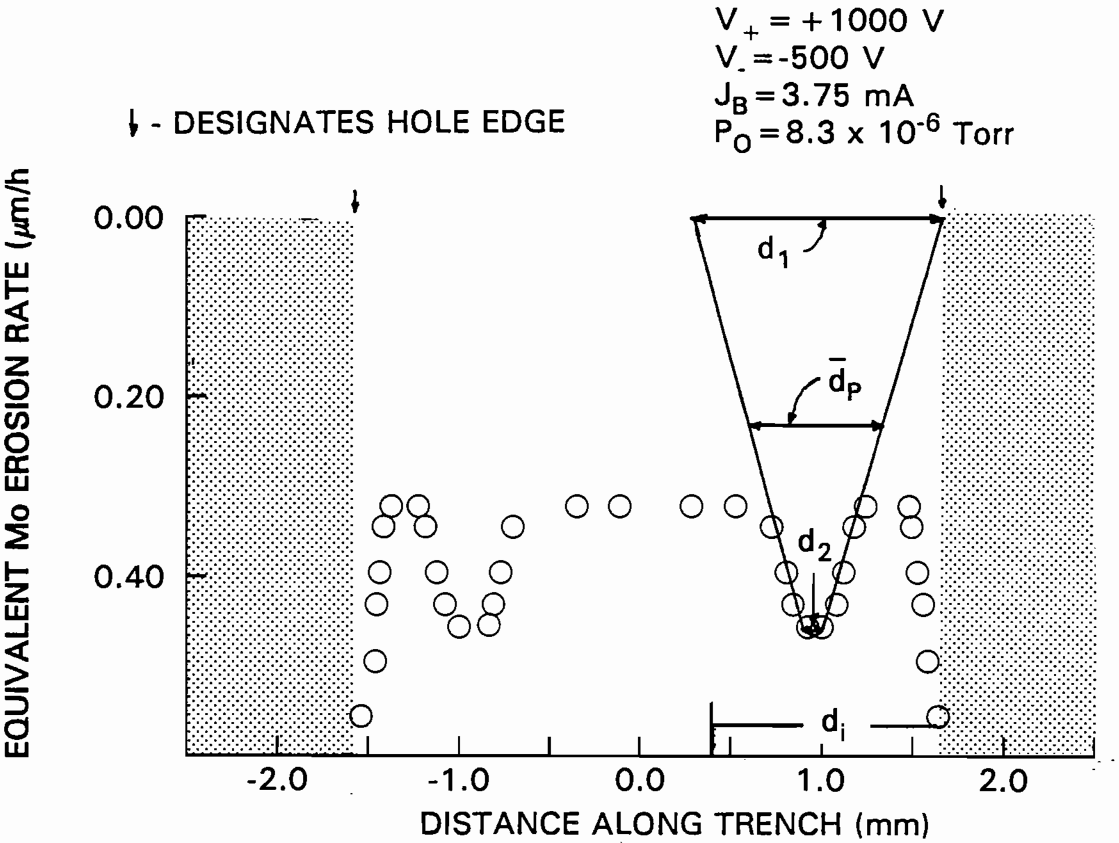

a. Across Two Pits and Along Trench

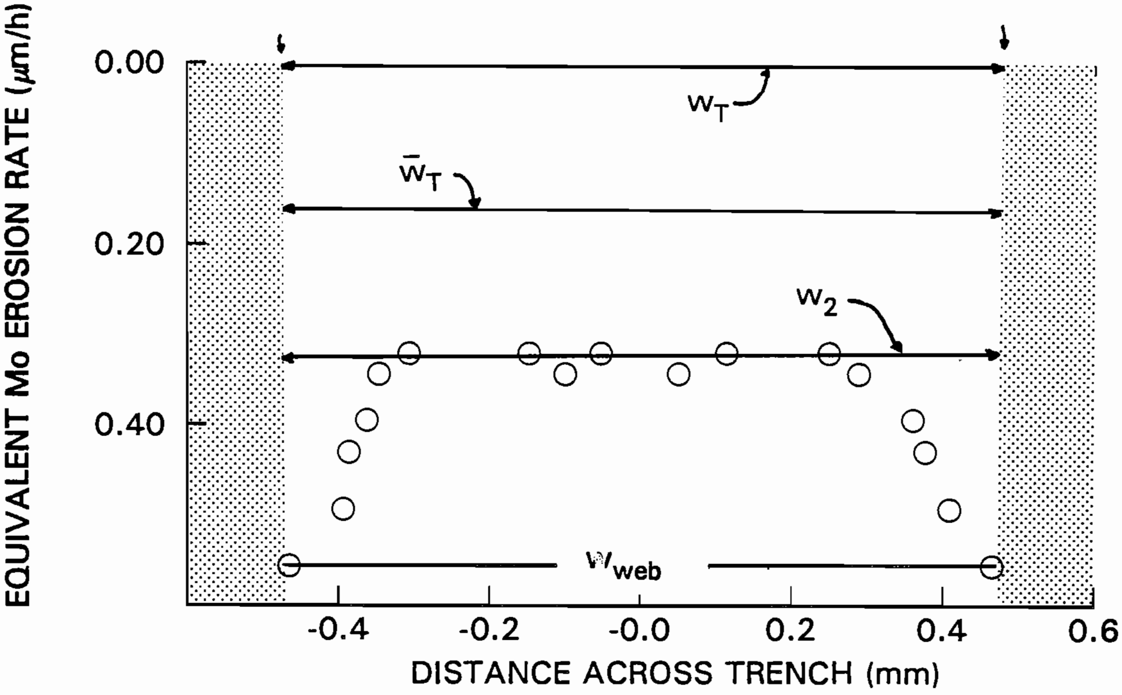

b. Across Trench at Its Midpoint

Fig. 19 Erosion Rate and Shape Profiles at 3.75 mA Beam Current

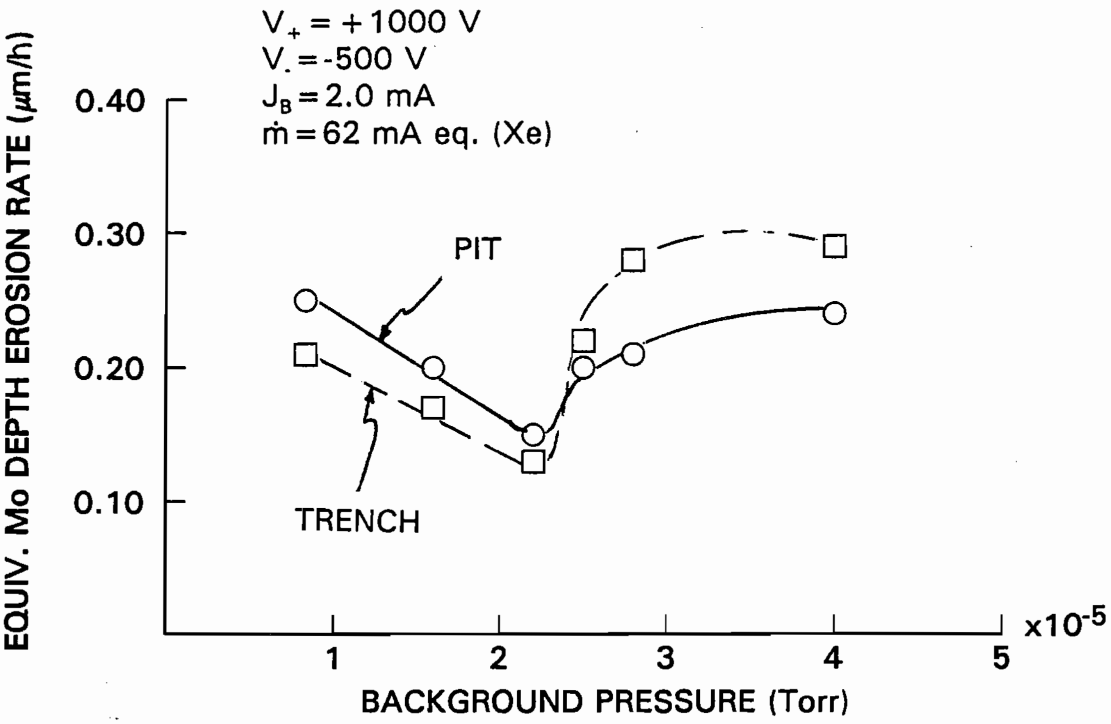

a. Pit and Trench Depth-Erosion Rates

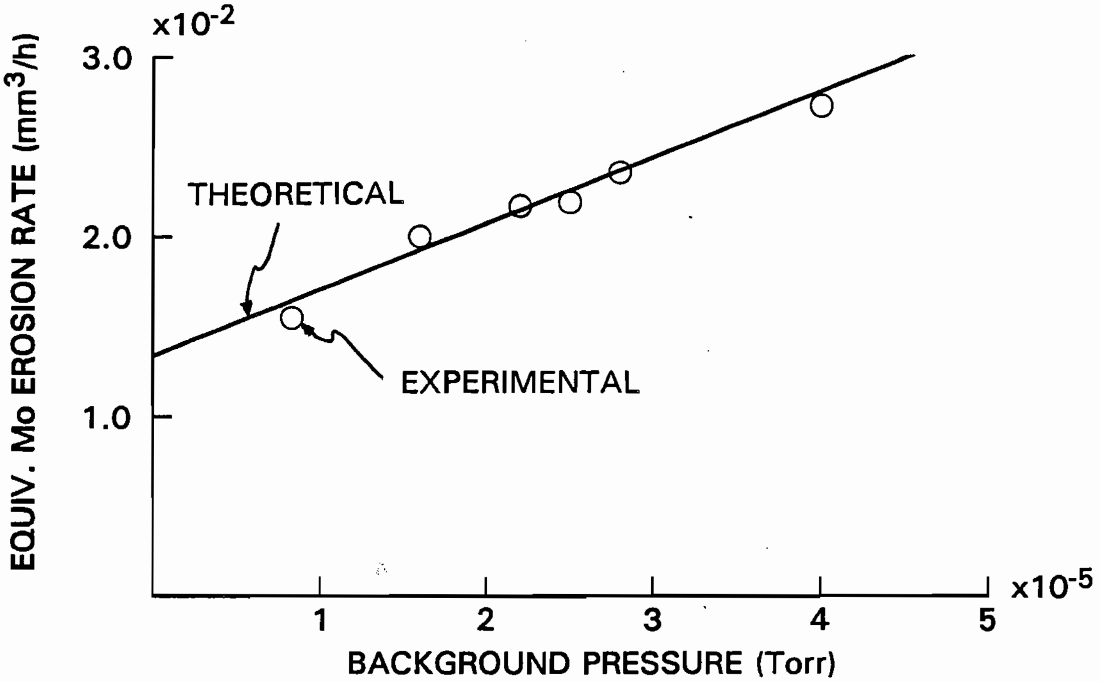

b. Experimental and Theoretical Volumetric-Erosion Rates

Fig. 20 Effect of Background Pressure on Equivalent Molybdenum Erosion Rates

~2.2 x 10^{-5} Torr. The trench depth-erosion rate becomes greater than the pit depth-erosion rate above 2.2 x 10^{-5} Torr, and both pit and trench depth-erosion rates level off at pressures above 2.8 x 10^{-5} Torr. Recall that it was expected, based on the impingement current results alone, that the pit and trench depth-erosion rates would increase linearly with background pressure. Since this behavior is not observed, it is evident that one of the parameters which effect the depth erosion rate (Eq. 2) must by changing. While pit and trench depth-erosion rates show complex behavior with increasing pressures, theoretical and calculated experimental volumetric erosion rates increase linearly between 8 x 10^{-6} and 4.0 x 10^{-5} Torr as shown in Fig. 20b. Again, calculated experimental molybdenum erosion rates are within ~10% of the theoretical values (based on measured impingement currents) and are in agreement with the impingement current trends shown in Fig 15a.

The pit and trench erosion proportionality factors are shown in Fig. 21a. From this plot is evident that the ratio between the pit and trench depth-erosion rates and the total experimental volumetric-erosion rates is not constant with background pressure as it was for beam current. This is due to the fact that one or more of the parameters describing depth-erosion rate are changing. For example, pit and trench impingement current density uniformity factors (f) shown in Fig. 21b show quite complex behavior with increases in background pressure. Both the pit and trench impingement current density uniformity factors vary in a similar manner fluctuating over about a 0.8 and 0.4 range, respectively, as pressure is varied.

The change in pit and trench shapes with background pressure can be seen in

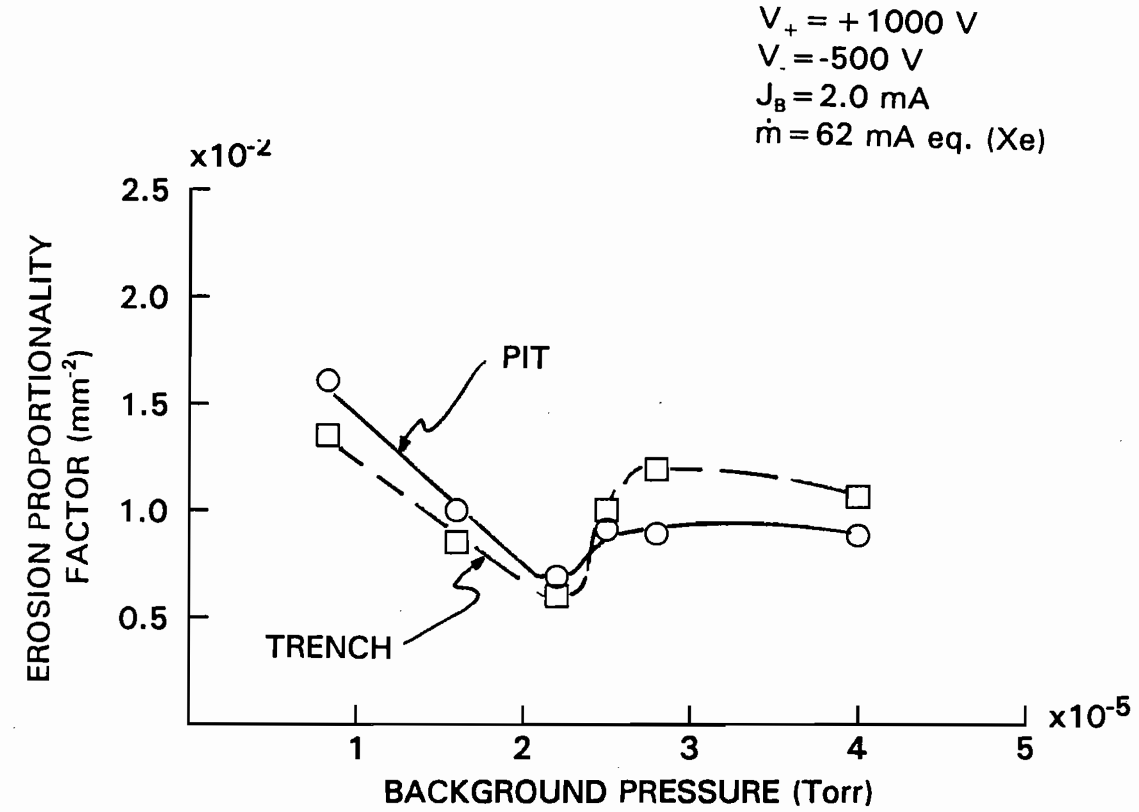

a. Erosion Proportionality Factors

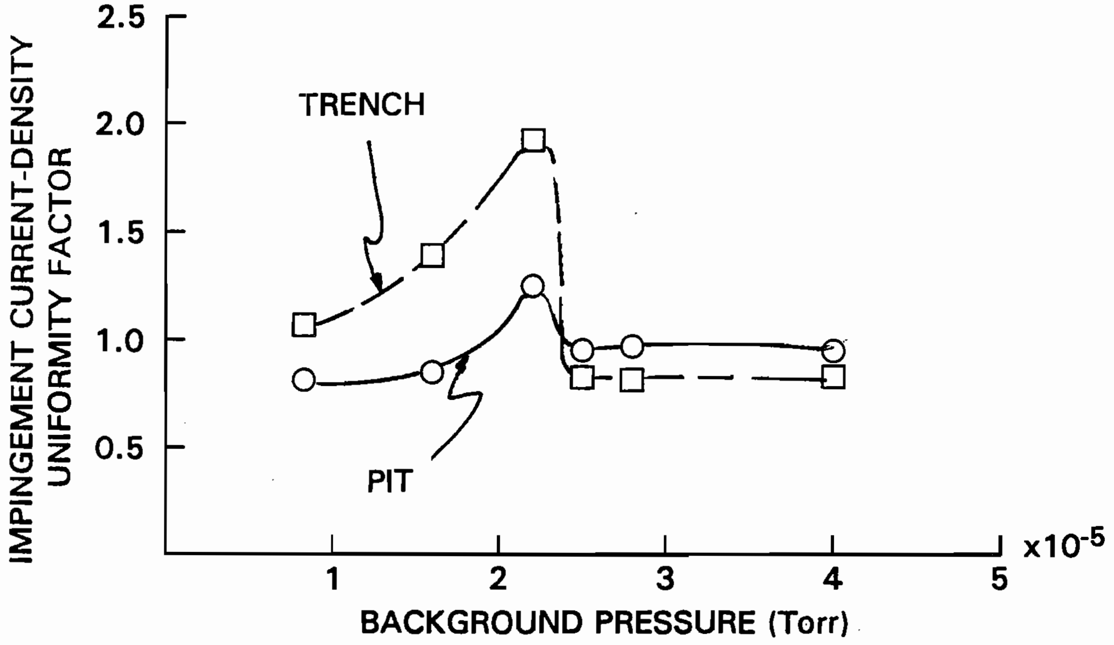

b. Impingement Current-Density Uniformity Factors

Fig. 21 Effect of Background Pressure on Pit and Trench Erosion shape factor plot in Fig. 22a. Both pit and trench factors remain relatively near 0.7 and 0.5, respectively, over the pressure range investigated. At pressures near 2.5×10^{-5} Torr, both pit and trench shape factors vary over about a 0.2 range as the background pressure is increased.

Another major factor which causes the depth-erosion rate to vary non-linearly is the relative balance of the erosion between the active beam and periphery (δ) as the background pressure is varied. This effect is shown in Fig. 22b where the ratio of periphery-to-total volumetric erosion rate is plotted against background pressure. The figure shows that as pressure is increased, the amount of erosion seen outside the active beam area dramatically increases until it approaches ~32% of the total erosion at 4×10^{-5} Torr. The extensive periphery erosion seen at higher background pressures is thought to be caused by the additional production of charge-exchange ions in the far-field region downstream of the thruster grids. This occurs because an increase in background pressure induces an increase in the production of far-field charge-exchange ions. These ions are created uniformly within the active beam area but unlike the near-field charge-exchange ions which are produced close to the grids, they are produced far from them. As a consequence, many of them escape the active beam area before they strike the grids. Their escape from the beam far from the grids is facilitated by an ambipolar electric field [17] which develops in the beam and is directed radially out from the beam centerline. The field develops because electrons tend to diffuse radially out of the plasma at a faster rate than the positive charge-exchange ions. This results in charge separation that induces the ambipolar field which retards the electron diffusion

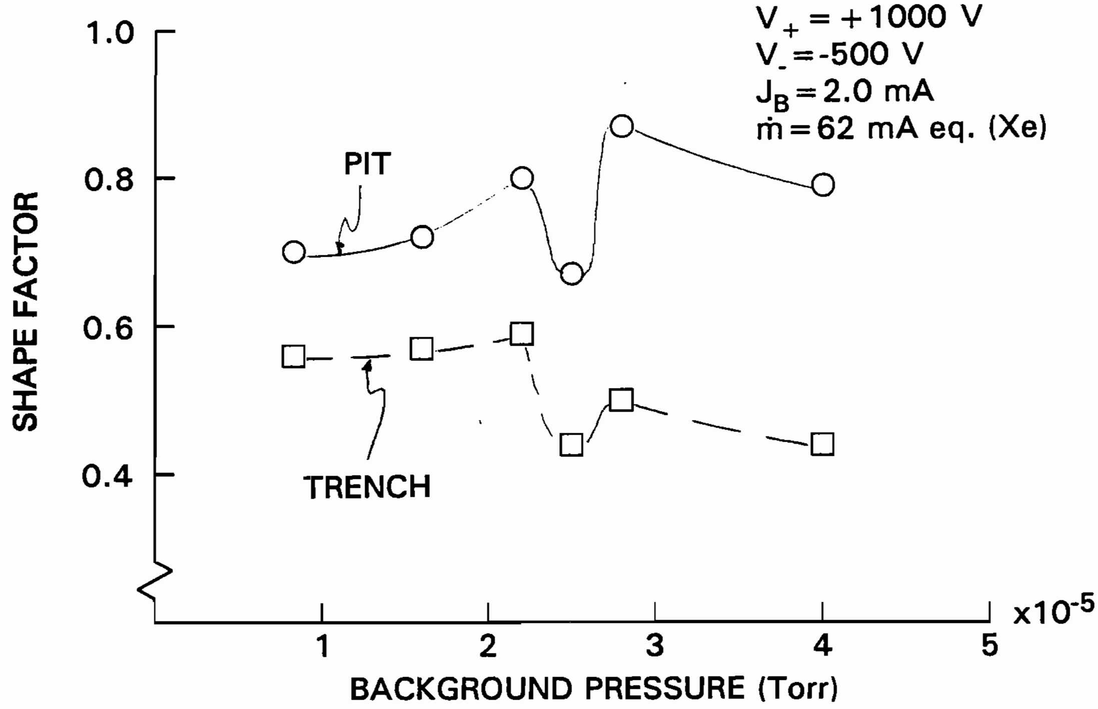

a. Pit and Trench Shape Factors

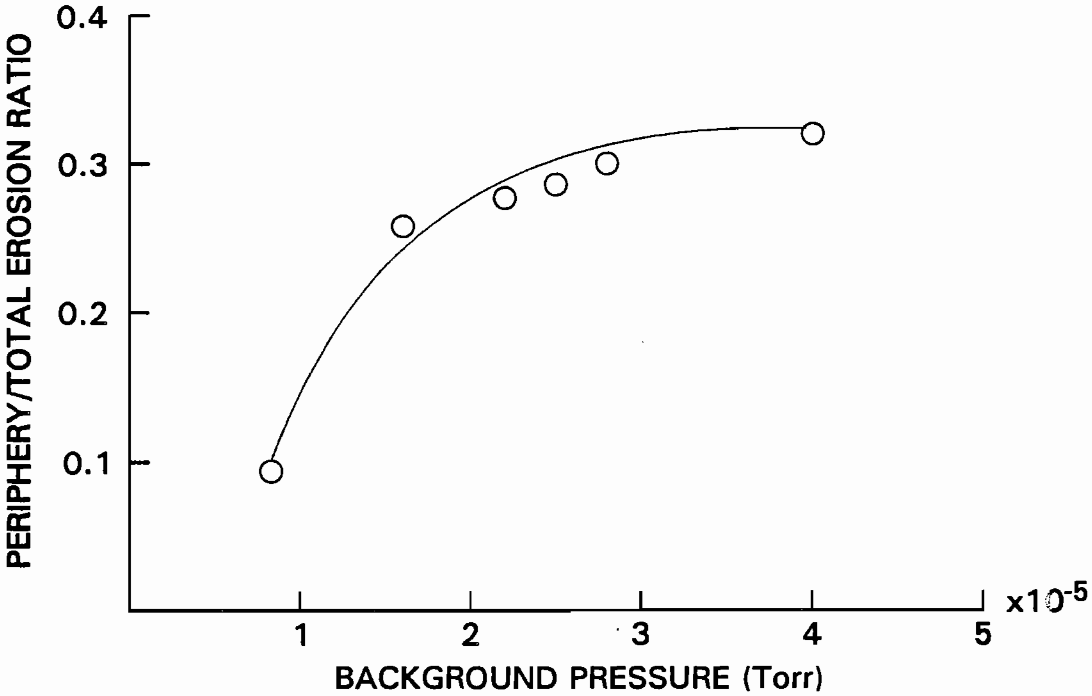

b. Ratio of Periphery-to-Total Erosion Rates

Fig. 22 Effect of Background Pressure on Accel-Grid Erosion and at the same time enhances the diffusion of the charge-exchange ions to the periphery of the beam. At greater background pressures, both electron diffusion and ion extraction rates are enhanced. Both the enhanced far-field charge-exchange ion production rate and the enhanced ambipolar diffusion may contribute to the increase in periphery erosion fraction shown in Fig. 22b. It is noteworthy that the results of Fig. 22b are consistent with those proposed from PIC (Particle In Cell) model by Polk and Brophy [9]. In addition, it appears that these results are also in agreement with lifetime tests performed at elevated background pressures which show a ring of erosion occurring just outside the active beam-area boundary [10].

Background-pressure-effect data have shown that because of changes in two factors which determine depth-erosion rates (δ and f), erosion-proportionality factors can show complex behavior. As a result, it is probably not good practice to predict grid lifetimes at a prescribed pressure on the basis of volumetric-erosion-rate measurements made at a pressure that is different from that where the grid will be operating.

Equivalent molybdenum depth-erosion rates were determined as a function of accel-grid potential from experimental measurements. The depth-erosion rates, which were calculated from measurements made at accel-grid potentials of -300, -500, and -750 V, are plotted in Fig. 23a. Both pit (open circles) and trench (open squares) depth-erosion rates decrease in a similar way with increasing accel-grid potential. Experimental volumetric-erosion rates based on erosion patterns (open circles) and measured impingement current (solid line) which decrease linearly from

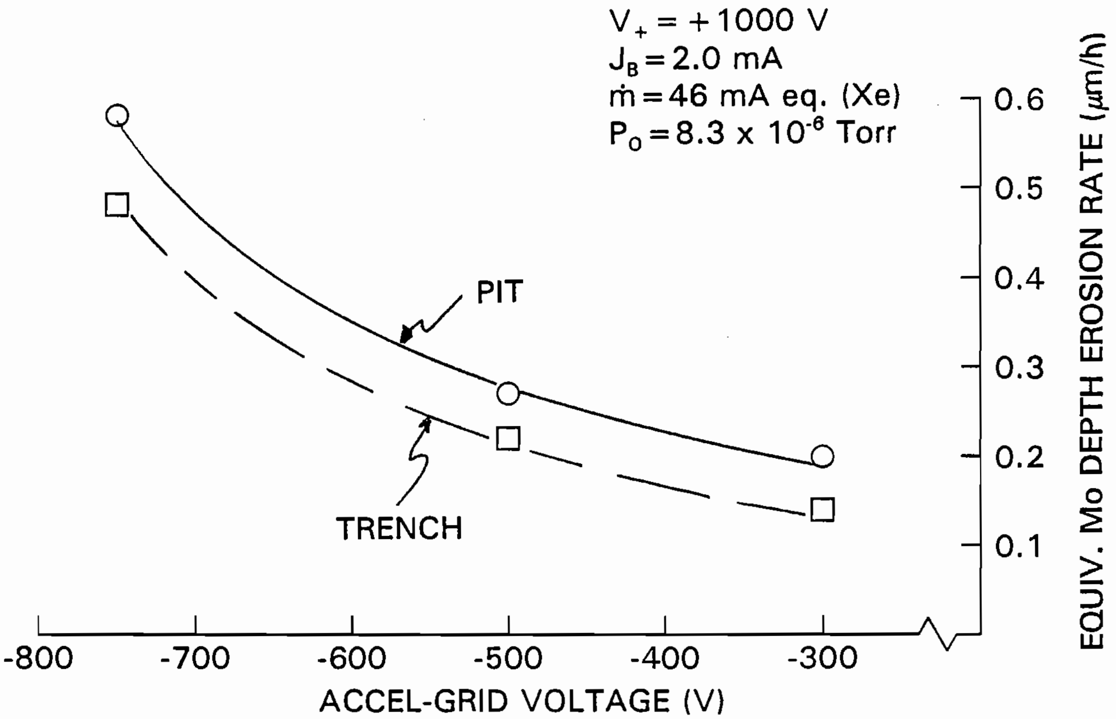

a. Pit and Trench Depth-Erosion Rates

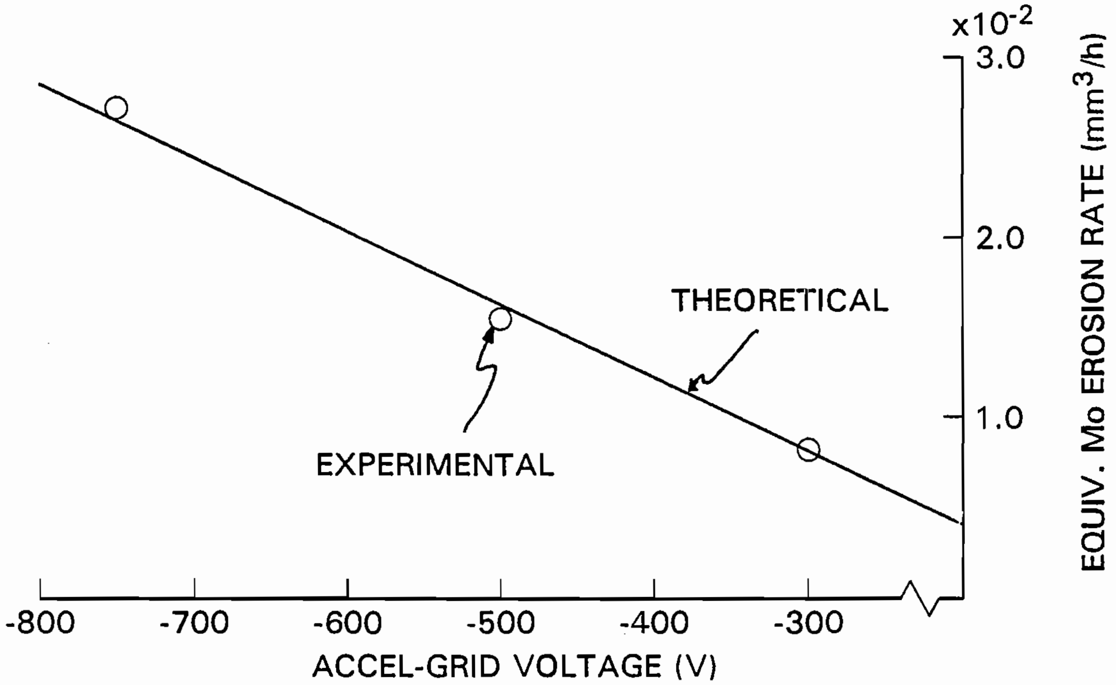

b. Experimental and Theoretical Volumetric-Erosion Rates

Fig. 23 Effect of Accel-Grid Voltage on Equivalent Molybdenum Erosion Rates

~2.8 x 10^{-2} mm^3/hour to ~8 x 10^{-3} mm^3/hour with increases in accel-grid potential as shown in Fig. 23b, are again in good agreement.

Erosion proportionality factors from the erosion rate data presented in Fig. 23 are shown in Fig. 24a for both the pits and trenches. Both pit and trench proportionality factors vary rather modestly ($\leq \pm 20\%$) about their mean values (~ 2.0 for the pit, and ~1.6 for the trench) over the range investigated. Because the periphery erosion was a small fraction of the total erosion ($\leq 4\%$) for all of the accel grid potentials investigated in these tests, Eq. 6 shows the variation must be due to changes in the impingement current density uniformity factor (f). Pit and trench impingement current density uniformity factors are shown in Fig. 24b to have median values of 1.2 x 10^{-2} and 7.0 x 10^{-3}, respectively, over the accel-grid voltage range investigated. These variances will assist in explaining the changes in depth-erosion rates and thus proportionality factors.

Accel-grid voltage effects on pit and trench shapes are shown in the shape factor plots of Fig. 25. Both pit and trench shape factors, which decrease gradually with initial increases in accel-grid voltage, show more substantial decreases with further accel-grid voltage increases. These trends indicate charge-exchange ions become more narrowly focussed into pits or trenches as accel-grid voltage magnitude is increased.

The relationship between accel-grid depth-erosion rates and the parameters which induce them, involve several competing factors which must be examined together to understand accel-grid voltage effects on depth-erosion rates. First, it has been shown that impingement current increases with increased accel-grid voltage

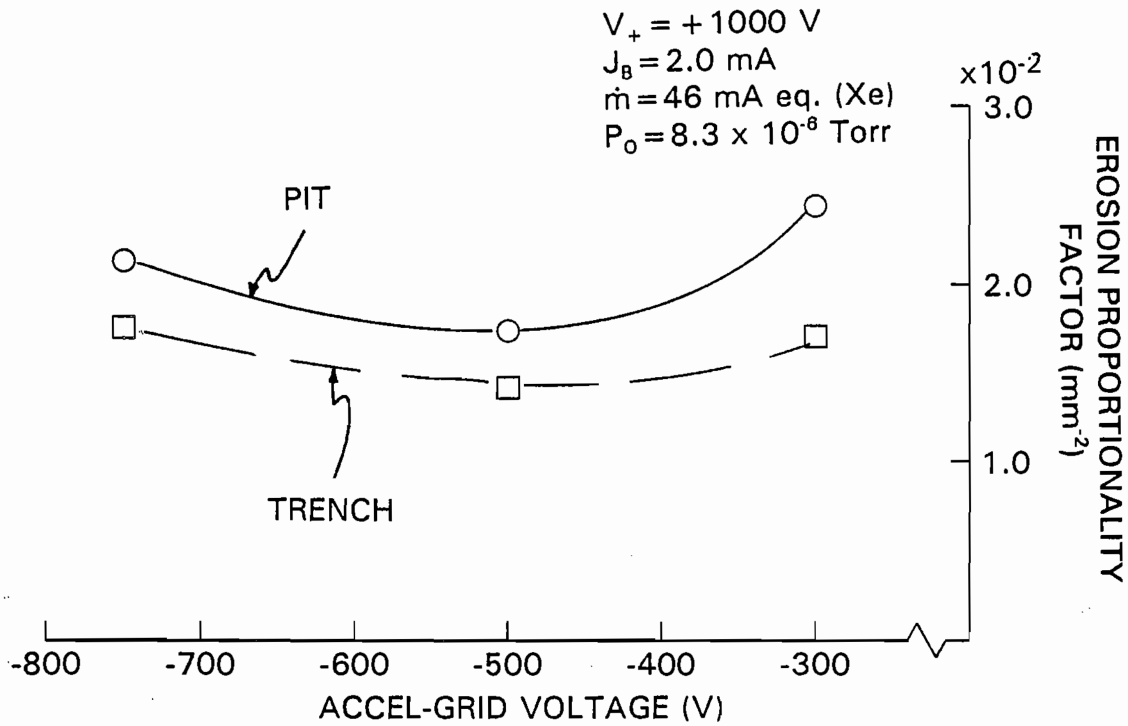

a. Pit and Trench Erosion Proportionality Factors

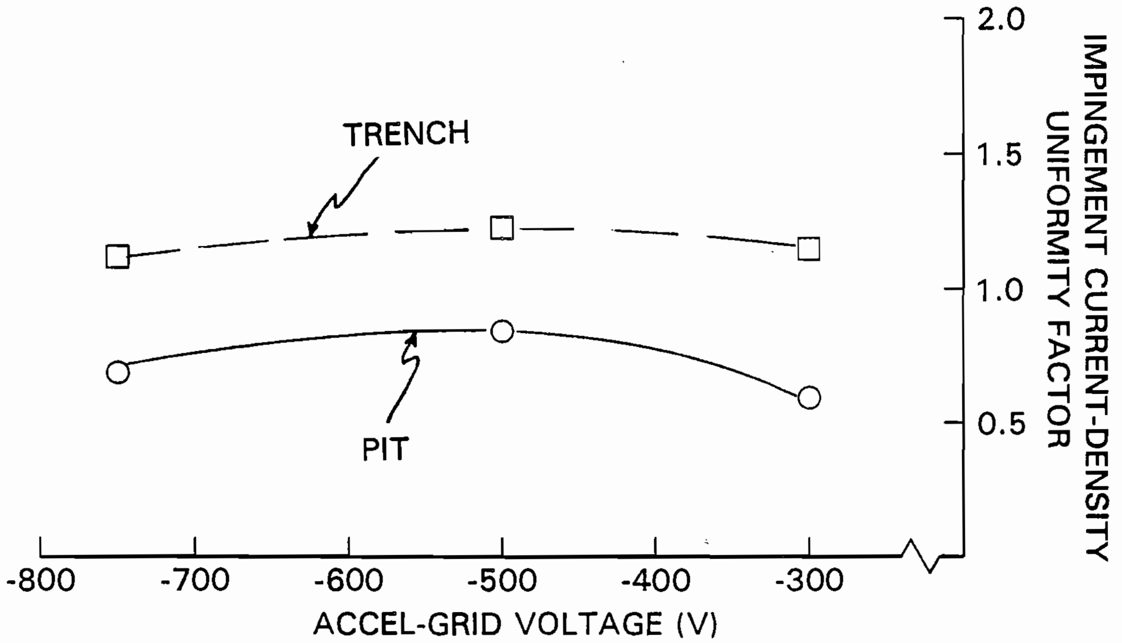

b. Pit and Trench Impingement Current-Density Uniformity Factors

Fig. 24 Effect of Accel-Grid Voltage on Accel-Grid Erosion

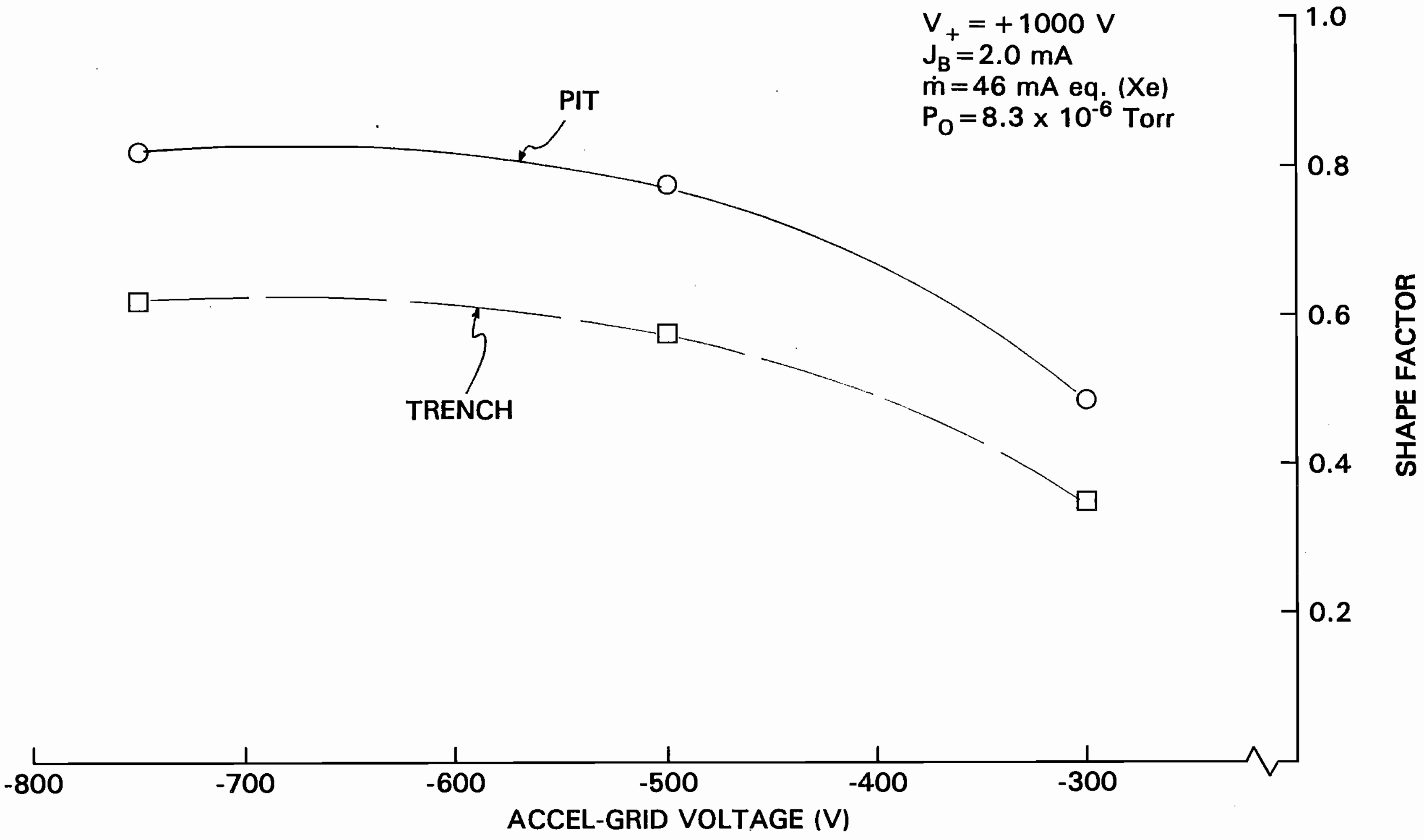

Fig 25 Effect of Accel-Grid Voltage on Pit and Trench Shape Factors

magnitude. From this alone, one would expect a linear increase in depth-erosion rates. Because periphery erosion was constant, there are only two factors which affect the depth-erosion rate namely 1) sputter yield, and 2) impingement current density uniformity factor. Depth-erosion rates increase as accel-grid voltages become more negative because both impingement current and sputter yield increase with accel-grid voltage magnitude. Thus, the combination of the three parameters which vary with increases in accel-grid voltage magnitude (impingement current, sputter yield, and impingement current density uniformity factor) lead to the depth-erosion rate profiles seen in Fig. 23a.

C. Data Comparison with Life Test Results

In order to evaluate the usefulness of the data developed in this report as a tool for predicting lifetimes of accel grids, the data were used to predict grid erosion at conditions close to those associated with a thruster life test. The usefulness would then be demonstrated comparing the measured sputter erosion on the life test grid with that predicted from the data. The life test selected for comparison was conducted on a 30 cm diameter 5kW xenon ion thruster [18]. The grid geometrical and operating conditions associated with a region on the life-tested grid for which measurements were available are listed in Table 2, along with the corresponding multilayer test conditions selected to agree as closely as possible with those for the life test.

Table 2

Life-Test and Multi-Layer Test Conditions

Parameter	Life Test	Multi-Layer Test
Screen Grid Potential (V)	1500	1000
Accel-Grid Potential (V)	-330	-300
Beamlet Current Per Aperture (A)	2.2×10^{-4}	1.05×10^{-4}
Impingement Current Per Aperture (μA)	1.2	1.2
Neutral Flow Rate Per Aperture (mA)	0.224	2.42
Ambient Pressure (Torr)	1.27×10^{-5}	8.3×10^{-6}
Screen Grid Hole Diameter (mm)	1.90	1.98
Accel-Grid Hole Diameter (mm)	1.14	1.47
Screen Grid Thickness (mm)	0.36	0.25
Accel-Grid Thickness (mm)	0.36	0.25
Grid Spacing (mm)	0.76	0.66

As these data show, the multi-layer test conditions were selected so the impingement current per hole was the same and the accel-grid voltage and ambient pressure were as close as possible to corresponding values for the life test. This was done by assuming the impingement-current density profile has the same shape as the measured beam-current density profile. The life test, which was conducted for 1160 hours, yielded the erosion profile (through two pits and along a trench) that is shown in Fig. 26a. The computed profile, which is shown in Fig. 26b, was obtained by multiplying depth-erosion rates at each point of measurement for the multi-layer test profile by 1160 hours. A comparison for the profiles in Fig. 26 show the pit erosion depths are similar but the trench depth for the life test is about one-third of that from the multilayer test.

Phenomena that could contribute to differences between life-test and predicted results include: 1) impinging-ion scattering mitigated by an order-of-magnitude lower neutral propellant flow per aperture for the life test, 2) re-sputtering necessitated by atoms from the life-test grid that were sputtered onto opposing surfaces rather than being ejected, and 3) impinging-ion focusing affected by small differences in grid geometries and/or the greater screen-grid potential for the life test. It is currently thought, however, that the much higher neutral flow rate per aperture in the multilayer test will have a predominant effect. Specifically, higher neutral flow rates will affect the charge-exchange density just downstream of the grids, which directly affects the equi-potential lines. Changes in the equi-potential lines will effect the trajectories of impinging ions, thereby changing the distribution of the erosion.

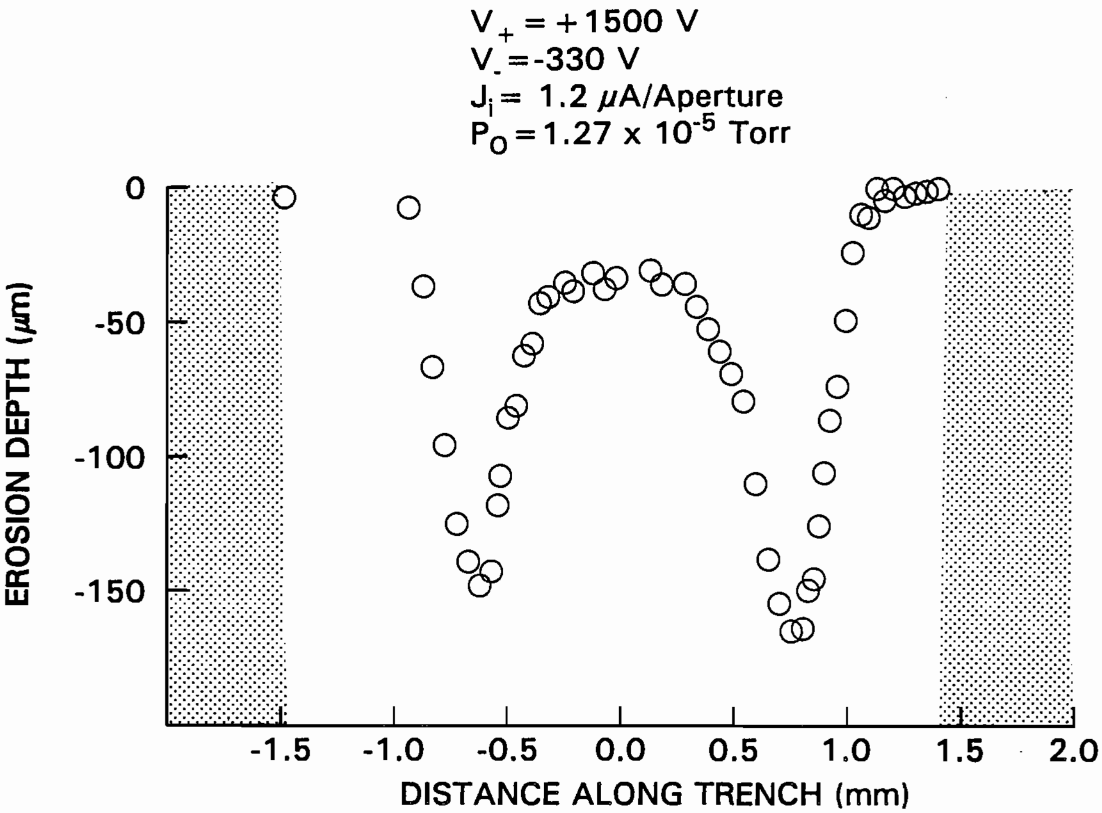

a. Erosion-Depth Profile from 30 cm Grid Lifetime Test (1160 hrs.)

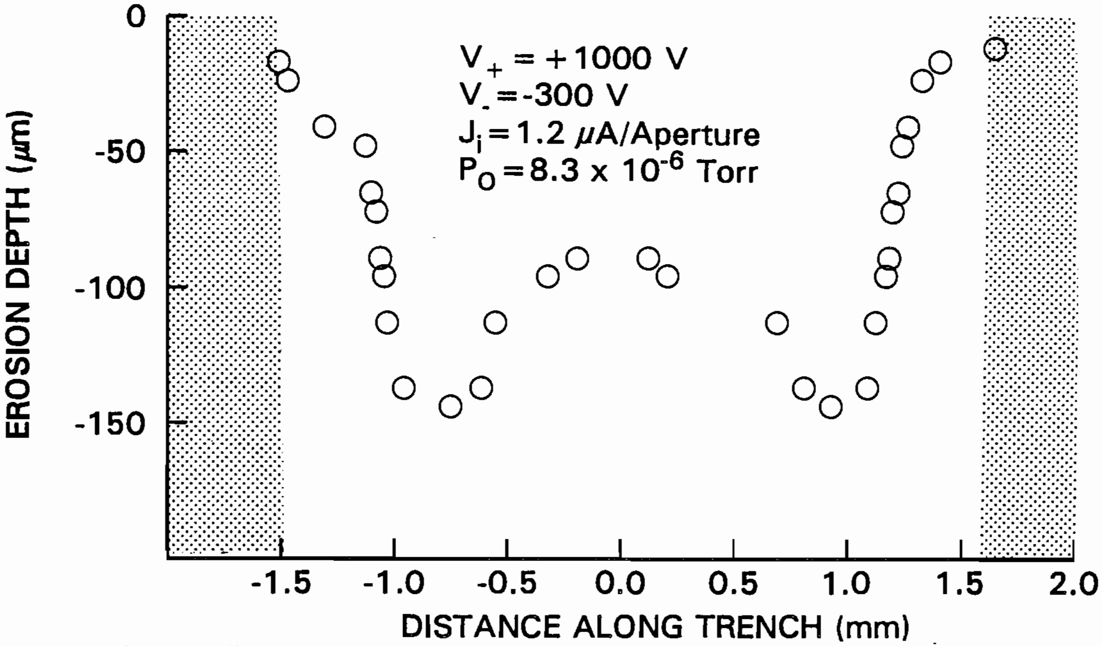

b. Predicted Erosion-Depth Profile Based on Measured 19-Hole SHAG Rates Applied for 1160 hrs.

Fig. 26 Comparison of Computed and Measured Erosion Profiles

If the multilayer test could have been operated with a lower neutral propellant flow rate, and could account for material which is re-deposited within the pits and trenches, it is expected the two profiles of Fig. 26 would be in better agreement.

V. Conclusions

Experimental data and theoretical calculations presented in this thesis have shown that charge-exchange ions impinging on the downstream surfaces of accel grids cause sputter erosion. The multilayer erosion technique described can be used to study the effect of ion-thruster operating conditions and background pressure on accel-grid erosion rates. Erosion volumes measured from these tests were found to agree with theoretical erosion volumes calculated using measured impingement currents. In addition, erosion profiles predicted from the multilayer erosion technique were found to resemble profiles of an actual accel-grid lifetime test conducted for 1160 hours. Hence, it is argued that the multilayer experimental method used to measure the erosion rates is valid.

The effects of beam current, background pressure, and accel-grid potential on accel-grid erosion have been examined. The resulting data as well as erosion data measured by other researchers show the erosion is concentrated in a pattern of pits and trenches. Measured volumetric-erosion rates and theoretical volumetric-erosion rates (based on measured impingement current) were found to increase linearly with: 1) beam current (to the point of direct impingement), 2) background pressure, and 3) accel-grid voltage magnitude. Depth-erosion rates were, however, found to vary differently as these operating conditions were changed. Specifically, depth-erosion rates for both pits and trenches increased linearly with beam current. Increases in accel-grid voltage magnitude, on the other hand, induced a greater-than-linear increase in depth-erosion rates (greatest increases at higher accel-grid voltage magnitudes). This greater-than-linear increase can be explained by the increase in sputter yield that accompanies an increase in this voltage magnitude. Depth-erosion rates in the pit and trench show complex behavior with increasing background pressures. It appears that this behavior is a consequence of two competing effects induced by pressure changes. Specifically, background pressure increases induce an increase in impingement current and at the same time, some of the impinging ions are redirected both within the active beam and away from the active grid area beyond the beam edge (the periphery). Thus, erosion seen outside the active area of the grid becomes quite severe (approaching ~32% of the total erosion at the highest pressure used in these studies). A significant redistribution of ions within the active beam area was also observed as ambient pressure was varied. This shift in erosion from within the active beam area to the periphery, which was observed as background pressure was increased, did not appear to be affected by changes in accel-grid voltage at a low pressure.

Depth-erosion rates can depart from linear dependencies with impingement current because impingement-current density distributions over the accel-grid surface change as operating parameters are changed. This variation in uniformity can be described through the use of impingement current density uniformity factors which relate average impingement current densities to peak ones. Pit and trench uniformity factors are shown to vary with all of the operating conditions investigated, but they show minimal variation with beam current. Depth-erosion rates do not scale in direct proportion with volumetric erosion rates (i.e. with impingement currents) because of variations in the periphery erosion fraction, impingement current density uniformity factors, and the sputter yields that accompany changes in beam current, accel-grid voltage and ambient pressure.

In general, depth-erosion-rate data obtained by linear scaling with beam-current-induced changes in impingement current should be accurate to within ~10% up to the point of direct impingement. Since the current-density distribution also remains relatively constant as accel-grid voltage is varied, linear scaling that accounts for accel-grid-voltage-induced changes in both sputter yield and impingement current should be accurate to within ~20%. Changes in ambient pressure causing a redistribution of impingement-current densities within the active beam area and to the periphery of this area are complex and not understood well. The data presented show that linear scaling based on ambient-pressure-induced changes in impingement current cannot be justified.

VI. Future Work

Although work presented in this thesis produced valuable results in understanding accel-grid erosion mechanisms, the effects of only three parameters were investigated. To broaden the knowledge of operating condition effects on accel-grid erosion characteristics, many more parameters must be investigated. For instance, initial tests used for proof of concept for the experimental method used in this research were performed on accel grids with various geometries. Initial results indicate that changes in accel-grid open area fraction and aperture diameter can lead to different erosion characteristics at similar operating conditions. Furthermore, screen-grid potential and propellant flow rate effects on accel-grid erosion should be investigated.

It should be noted that this experimental method is not limited to use on traditional accel-grid geometries. Specifically, this method could also be applied in investigating erosion patterns for recently designed grids made of carbon-carbon composite and having long thin-slit apertures [19]. As accel-grid designs evolve using different materials and geometries, the experimental procedure described in this thesis will prove to provide great amounts of information concerning accel-grid erosion characteristics.

VII. References

1. Aston, G., "Electric Propulsion: A Far Reaching Technology," AIAA Paper No. 85-2028, 18th International Electric Propulsion Conference, Alexandria, VA., Sept. 30 - Oct. 2, 1985.

2. Atkins, K.L., "Mission Applications of Electric Propulsion," AIAA Paper No. 74-1085, AIAA/SAE 10th Propulsion Conference, San Diego, CA, Oct. 21-23, 1974.

3. Sauer, C., "Application of Solar Electric Propulsion to Future Planetary Missions," AIAA Paper No. 87-1053, 19th International Electric Propulsion Conference, Colorado Springs, CO, May 11-13, 1987.

4. Jones, R.M., "A Comparison of Potential Electric Propulsion Systems for Orbit Transfer," AIAA Paper No. 82-1871, 16th International Electric Propulsion Conference, New Orleans, LA, November 17-19, 1982.

5. Free, B.A., "Economic Tradeoff Studies for Electric Propulsion Missions on Communications Satellites," AIAA Paper No. 71-683, 7th International Electric Propulsion Conference, Salt Lake City, UT., June 14-18, 1971.

6. Brophy, J.R., Pless, L.C.,Mueller,J.,and Anderson, J.R.,"Operating Characteristics of a 15-cm dia. Ion Engine for Small Planetary Spacecraft," IEPC 3-110, 23rd International Electric Propulsion Conference, Seattle, WA, Sept 13-16, 1993.

7. Rawlin, V.K., "Erosion Characteristics of Two-Grid Ion Accelerating Systems," IEPC 93-175, 23rd International Electric Propulsion Conference, Seattle WA. Sept. 13-16, 1993.

8. Patterson, M.J., Rawlin, V.K., Sovey, J.S., Kussmaul, M.J., Parkes, J., "2.3 kW Ion Thruster Wear Test," AIAA Paper No. 95-2516, 31st Joint Propulsion Conference, San Diego, CA, July 10-12, 1995.

9. Polk, J.E., Brophy, J.R., Wang, J., "Spatial and Temporal Distribution of Ion Engine Accelerator Grid Erosion," AIAA Paper No. 95-2924, 31st Joint Propulsion Conference, San Diego, CA, July 10-12, 1995.

10. Brophy J.R. and Pless, L., "Test-to-Failure of a Two-Grid, 30-cm dia. Ion Accelerator System," IEPC 93-172, 23rd International Electric Propulsion Conference, Sept. 13-17, 1993, Seattle, WA.

11. Monheiser, J.M., "Development and Verification of a Model to Predict Impingement Currents for Ion Thrusters," NASA CR-195322, April 1994.

12. Beattie, J.R., "Endurance Test of a 30-cm Diameter Engineering Model Ion Thruster", NASA CR-168132, June 1982.

13. Wilbur, P.J. and Buchholtz, B.W., "Surface Engineering Using Ion Thruster Technology," AIAA Paper No. 94-3235, 30th Joint Propulsion Conference, Indianapolis, IN, June 27-29, 1994.

14. Kerslake, W.R. and Ignaczak, L.R., "Development and Flight History of SERT II Spacecraft," NASA Technical Memorandum 105636, 28th Joint Propulsion Conference and Exhibit, Nashville, TN, July 6-8, 1992.

15. "Product and Vacuum Technology Reference Book," Leybold, Heraeus Inc., 1993, pp. 48-55.

16. Hudson, W.R., "Ion Beam Texturing," NASA Technical Memorandum X-73470, 3rd Vacuum Symposium, Chicago, IL, Sept. 21-24, 1976.

17. Holy, E.H. and Haskell, R.E., Foundations of Plasma Dynamics, MacmillanCo., NY, 1965, pp. 187-190.

18. Patterson, M.J. and Verhey, T.R., "5kW Xenon Ion Thruster Lifetest", AIAA Paper 90-2543, 21st International Electric Propulsion Conference, Orlando, FL, July 18-20, 1990.

19. Meserole, J.S. and Rorabaugh, M.E., "Fabrication and Testing of 15-cm Carbon-Carbon Grids with Slit Apertures", AIAA Paper 95-2661, 31st Joint Propulsion Conference, San Diego, CA, July 10-12, 1995.

20. Wehner, G.K., "Sputtering Yield Data in the 100-600 eV Energy Range," General Mills Report 2309, July 15, 1962.

VIII. Appendix A: Development of Volumetric Erosion Rate Equations

Total volumetric accel-grid erosion rate can be broken down into three separate terms pertaining to 1) pits, 2) trenches, and 3) the periphery. These terms can be evaluated experimentally and their sum can be divided by the test time to obtain the volumetric sputtering rate. This rate should be equal to the volumetric rate of grid material removal given by the product of the ion arrival rate, the sputter yield, and the volume associated with each sputtered atom. This relationship is given in Eq. A1 as

$$\sum_{\text{pits}} \frac{V_{\text{pits}}}{t} + \sum_{\text{trenches}} \frac{V_{\text{trenches}}}{t} + \frac{V_{\text{periphery}}}{t} = \frac{S(\epsilon) m_A J_i}{e\rho} , \qquad \text{(A1)}$$

where J_i is the impingement current and $S(\epsilon)$, m_A, and ρ are the sputter yield, atom mass, and density, respectively for the accel-grid material. If the pits, trenches, and periphery erosion are modeled properly, the two sides of Eq. A1 should agree.

A. Pit Equation Development

The erosion volume for one pit is modeled as the frustrum of an inverted right circular cone with larger and smaller base diameters d_1 and d_2, respectively. Thus, the volume of material removed in one pit is given in Eq. A2 as

$$V_{\text{pit}} = \left[\frac{1}{12}\pi h_p (d_2^2 + d_1 d_2 + d_1^2)\right] , \qquad \text{(A2)}$$

where h_P is the depth of the pit.

B. Trench Equation Development

Trench erosion volume is found by multiplying the length of the trench ℓ_T by its cross sectional area. Modeling the trench as trapezoidal in cross section with larger and smaller base widths of w_T and w_2, respectively, and a trench height h_T, the volume removed from a single trench is given by

$$V_{trench} = \left[\frac{1}{2}\ell_T h_T (w_T + w_2)\right] . \qquad \text{(A3)}$$

Trapezoidal bases w_T and w_2 are both found experimentally and the length ℓ_T is calculated using the distance between the outer diameters of two pits. Figure 1A shows a partial sketch of an accel grid labeled with several dimensions for use in developing the equation for trench length. Applying the law of cosines to the triangle connecting two pit centers and the center of an aperture, the equation shown in Fig. 1A is found. Solving this equation for trench length and simplifying gives

$$\ell_T = \frac{d_A}{2} + \frac{d_i}{2} - d_1 , \qquad \text{(A4)}$$

where d_A and d_1 are the aperture and pit diameters, respectively. The variable d_i is the diameter of a circle inscribed between three apertures (shown by the dashed circle) and therefore is a function of accel-grid geometry only. The value of d_i in terms of these accel-grid geometry variables has been used in the development of pit shape factor.

C. Periphery Equation Development

Periphery erosion volumes are modeled as right-triangular in cross section as

$$(l_T + d_1)^2 = 2\left(\frac{d_A}{2} + \frac{d_i}{2}\right)^2 (1 - \cos(60°))$$

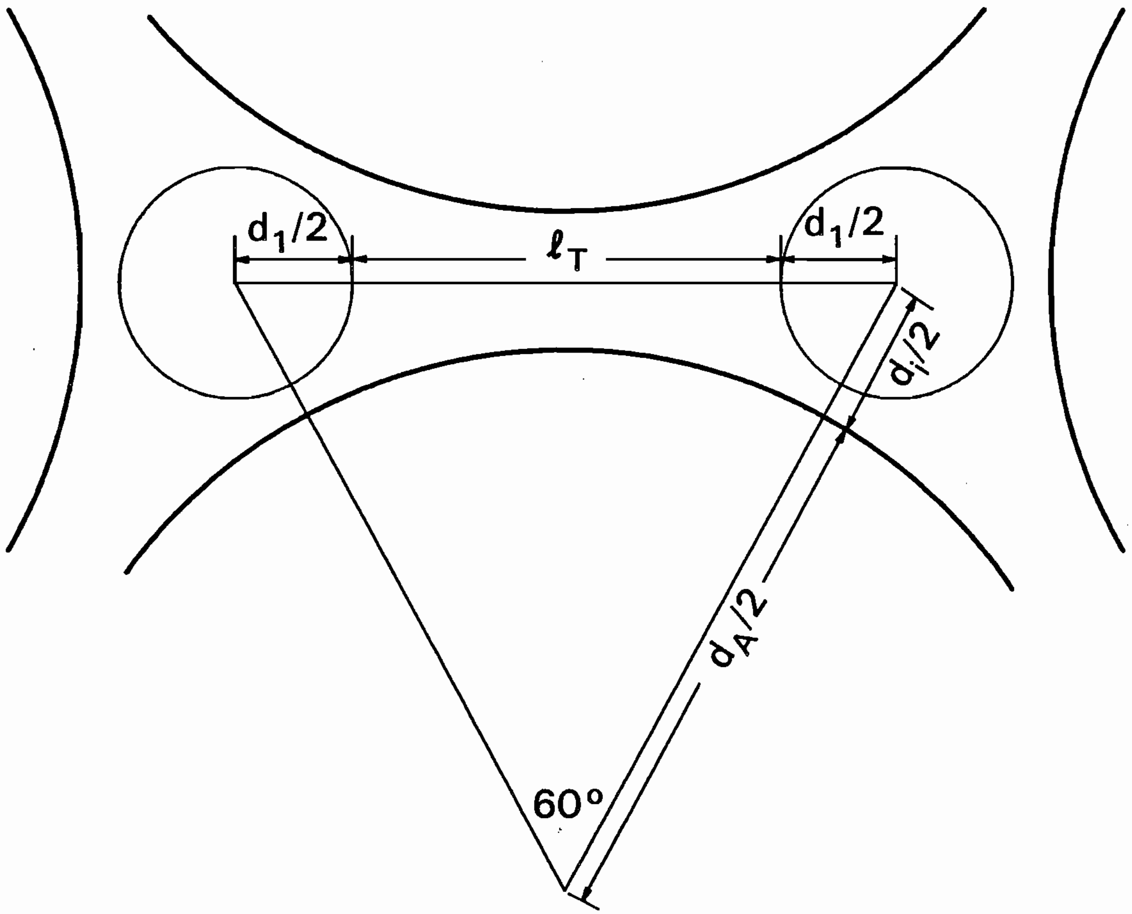

Fig. 1A Accel-Grid Trench-Geometry Dimension Relationships suggested in Fig. 2A for a sixth of the periphery of the 19-hole SHAG grid set. The two regions just outside of the active beam (Region 1 and Region 2) represent the corresponding periphery erosion areas. Also shown in Fig. 2A are cross-sectional views of the shaded regions along the lines X - X′ and Y - Y′, respectively. The depth and width of the cross section for Region 1 are h_{per} and w_{per}, respectively. The volume removed in Region 1 can be found by multiplying the area of the right-triangular cross section by the length of Region 1. The length of Region 1 is simply found from the geometry of the accel grid is given by

$$\ell_E = d_A \left(\frac{2\pi}{\sqrt{3}\phi_A} \right)^{\frac{1}{2}} , \qquad \text{(A5)}$$

where d_A and ϕ_A are the aperture diameter and open area fraction of the accel grid, respectively. Hence, the volume removed from region 1 is given as

$$V_{\text{Region 1}} = \frac{1}{2} w_{per} h_{per} \ell_E \ . \qquad \text{(A6)}$$

Similarly, from the geometry of region 2 the depth and width of the erosional cross section along Y - Y′ are h_{per} and w_{per}, respectively. Thus the volume removed within region 2 is found to be

$$V_{\text{region2}} = \frac{\pi}{3} \int_{x}^{x+w_{per}} r \ h \ dr, \qquad \text{(A7)}$$

where $x=(d_A+d_i-d_1)/2$, and $h=(-w_{per}/x)-(h_{per}/w_{per})r$. Summing the total amount of grid

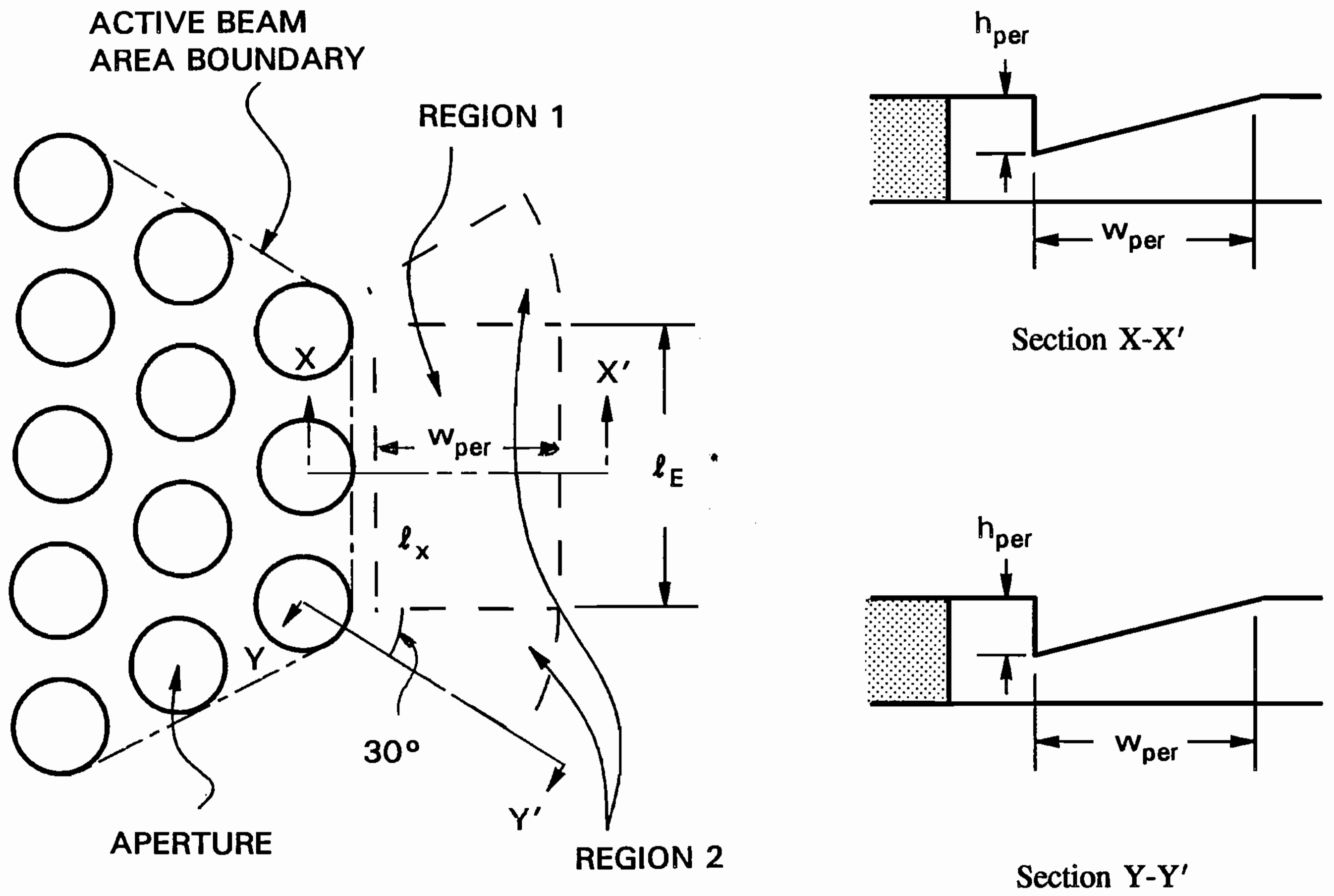

Section X-X′

Section Y-Y′

Fig. 2A Accel-Grid Periphery Model Dimensions material removed outside the active beam area (six region 1 and region 2 areas) the total periphery erosion volume is found.

D. Shape Factor Development

Recall that to describe ion-impingement focusing effects in the pit and trench areas, pit and trench shape factors were developed. Specifically, pit shape factor was defined as the full-cone frustrum width at half depth $\bar{d}_P$ divided by the maximum possible pit diameter d_i. Similarly, trench shape factor was defined as the full trapezoidal width at half the depth $\bar{w}_T$ divided by the maximum possible trench width w_{web}.

A partial sketch of an accel-grid consisting of three accel-grid apertures of diameter d_A equally separated by a distance ℓ_C is shown in Fig. 3A. Several other dimensions are labeled in Fig. 3A for use in finding shape factor parameters in terms of accel-grid geometry. The circle of diameter d_i inscribed between the three accel-grid apertures and represents the maximum possible pit size. From observation of the geometry presented in Fig. 3A, the diameter d_i can be found in terms of the aperture center-to-center spacing (ℓ_C) and the accel-grid aperture diameter (d_A). It is given by

$$d_i = \frac{[\ell_C - d_A \cos(30°)]}{\cos(30°)} . \tag{A8}$$

The term ℓ_C in Eq. A9 can be expressed in terms of accel-grid aperture diameter and open area fraction (ϕ_A) as

$$\ell_C = \left[\frac{\pi}{4\phi_A \cos(30°)}\right]^{\frac{1}{2}} d_A . \tag{A9}$$

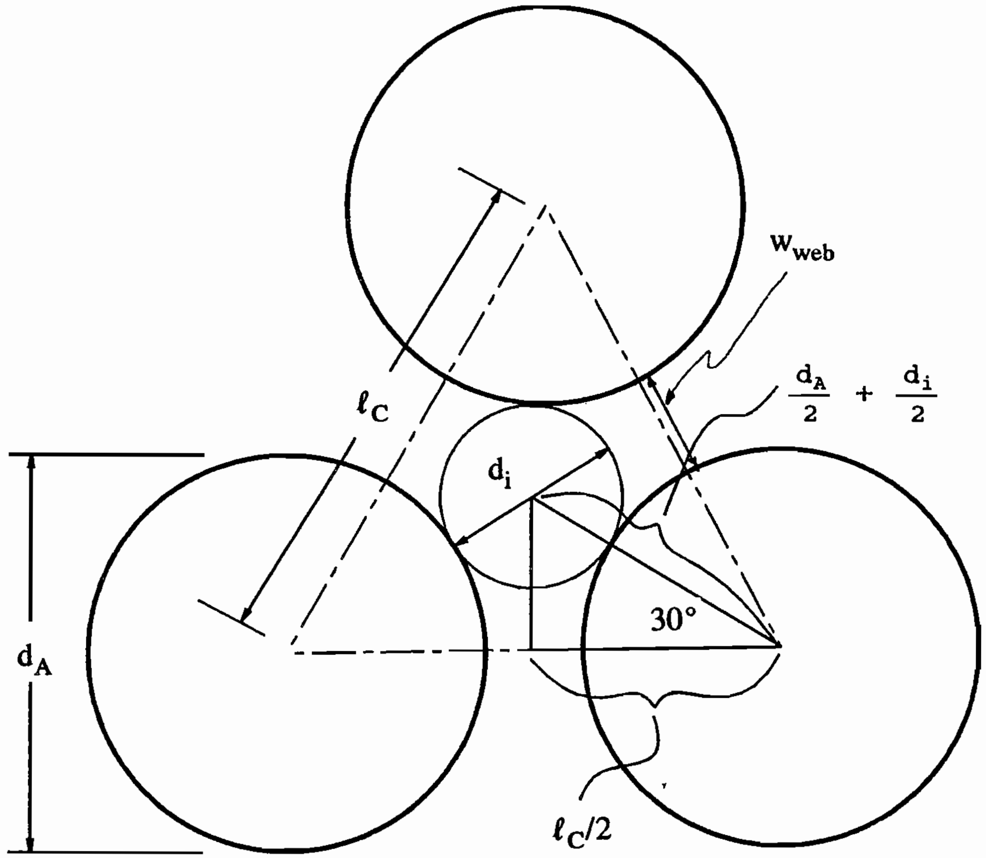

Fig. 3A Accel-Grid Pit-Geometry Dimension Relationships

Substituting Eq. A9 into Eq. A10, d_i is found to be

$$d_i = d_A \left[\sqrt{\frac{\pi}{4 \phi_A \cos(30°)^3}} - 1 \right], \tag{A10}$$

which is a function of accel-grid aperture diameter and open area fraction only. The pit shape factor can, therefore, be calculated by dividing measured values of d_P by the value given in Eq. A10.

The amount of accel-grid material between two apertures is labeled in Fig. 3A as the web width (w_{web}), and is simply given by ℓ_C - d_A. Thus, the web width can be expressed in terms of accel-grid aperture diameter and open area fraction by subtracting d_A from Eq. A9 and division by this width yields the trench shape factor.

IX. Appendix B: Sputter Yield Values

The sputter yield values used for the tests conducted in this paper are shown in Table 1B. The sputter yield values for molybdenum correspond to those for flat sheet molybdenum [20] at a specified energy. Sputter yield values for copper and stainless steel sputter coated onto surfaces were found experimentally. In particular, 500 Å of stainless steel (or copper) was sputtered onto a glass slide using the same coating apparatus and conditions used for the 19-hole SHAG accel-grids (outlined in Chapter III). The coated glass slide was then placed directly under a xenon ion beam at a specified energy (300, 500, or 750 eV) and a current density of 1 mA/cm^2 until the coating was removed. Knowing the current density, material properties, and the time it took to erode through the 500 Å layer, the sputter yield was calculated using Eqs 7 and 8.

Table 1B

Sputter Yields

	Sputter Yield (atoms/ion)		
Energy (eV)	Molybdenum	Sputtered SS	Sputtered Cu
300	0.50	0.30	0.73
500	0.91	0.45	1.20
750	1.40	0.50	1.38